Processes driving sea ice variability in the Bering Sea in an eddying ocean/sea ice model: anomalies from the mean seasonal cycle

Linghan Li · Arthur J. Miller · Julie L. McClean ·
Ian Eisenman · Myrl C. Hendershott

Abstract A fine-resolution (1/10°) ocean/sea ice model configured in the Community Earth System Model framework is compared with observations and studied to determine the basin-scale and local balances controlling the variability of sea ice anomalies from the mean seasonal cycle in the Bering Sea for the time period 1980–1989. The model produces variations in total Bering Sea ice area anomalies that are highly correlated with observations. Surface air temperature, which is specified from reanalysis atmospheric forcing, strongly controls the ice volume variability in this simulation. The thermodynamic ice volume change is dominated by surface energy flux via atmosphere-ice sensible heat flux, except near the southern ice edge where it is largely controlled by ocean-ice heat flux. While thermodynamic processes dominate the variations in ice volume in the Bering Sea on the large scale, dynamic processes are important on the local scale near ice margins (both oceanic and land), where dynamic and thermodynamic ice volume changes have opposite signs and nearly cancel each other. Ice motion is generally consistent with winds driving the flow, except near certain straits in the north where ice motion largely follows ocean currents. Two key climate events, strong ice growth with cold air temperature and northerly wind anomalies in February 1984 and weak ice growth with warm air temperature and southerly wind anomalies in February 1989, are studied here in detail. While the processes controlling the ice changes are generally similar to those in other years, these large events help reveal the characteristic spatial patterns of ice growth/melt and transport anomalies.

Responsible Editor: Pierre Lermusiaux

L. Li (✉) · A. J. Miller · J. L. McClean · I. Eisenman ·
M. C. Hendershott
Scripps Institution of Oceanography, University of California, San
Diego, La Jolla, CA 92093, USA
e-mail: li.linghan.li@gmail.com

1 Introduction

Sea ice variability plays an important role in how the physical environment impacts biology in the Bering Sea. The advance and retreat of sea ice has a major influence on biological productivity and the marine ecosystem of the eastern Bering Sea by affecting factors including light penetration through the ocean surface, water temperature, and the availability of substrate. Furthermore, the Bering Sea is where Pacific Ocean water flows into the Arctic Ocean. Thus, the sea ice and ocean conditions in the Bering Sea could affect the downstream Chukchi Sea and the Arctic Ocean and may play a role in the recent precipitous decrease in summer ice there (e.g., Fetterer et al. 2002, updated daily).

Sea ice in the Bering Sea exhibits significant seasonal, interannual, and decadal variability. The seasonal variation of sea ice in the Bering Sea is large. The maximum ice extent in winter can cover nearly the entire continental shelf; however, in the summer, the Bering Sea is essentially ice free (e.g., Fetterer et al. 2002, updated daily). The observed interannual variation of ice extent is about 25 % of the seasonal range (Niebauer 1983, 1998; Stabeno et al. 1998). The eastern Bering Sea showed the largest nonseasonal variation in sea ice extent during 1953–1977 among the marginal seas around the Arctic Ocean (Walsh and Johnson 1979). On longer timescales, the Bering Sea ice can be qualitatively described as having experienced several different regimes in recent decades: 1972–1976 was cold, 1977–1988 was warm, and 1989–2001 was cool (Stabeno et al. 2001). Interestingly, the winter sea ice cover in the Bering Sea has increased on average since 1979, while the sea ice cover in all seasons in

most of the rest of the Arctic has decreased (Fetterer et al. 2002, updated daily).

Both thermodynamic and dynamic processes contribute to the sea ice mass balance. Thermodynamic ice growth and melt is determined by heat fluxes between the ice and the atmosphere and between the ice and the ocean. Dynamic processes involve convergent or divergent ice motion causing the local ice volume to increase or decrease. Although the sea ice mass budget for the Arctic has been studied previously (Walsh et al. 1985; Zhang et al. 2000; Bitz et al. 2005; Holland et al. 2010), understanding of the thermodynamic and dynamic contributions to the ice volume change in the Bering Sea is limited (Walsh et al. 1985; Bitz et al. 2005; Zhang et al. 2010; Danielson et al. 2011; Cheng et al. 2014).

The observed winter climatology of sea ice cover in the Bering Sea has been described as a conveyor belt mechanism, where ice is formed in the north, drifts southward under the influence of northerly winds, and is melted by the ocean along the southern ice edge (Muench and Ahlnas 1976; Pease 1980). Li et al. (2014) quantified this mechanism using an ice-ocean model simulation, which also allowed for an explanation of the spatial structures of the seasonal variations. Li et al. (2014) show that modeled seasonal thermodynamic ice volume change is dominated by surface heat exchange with the atmosphere in the north and ice-ocean heat flux along the southern ice edge, with dynamic ice transport largely driven by wind stress.

The climate forcing of sea ice interannual variability in the Bering Sea has been studied extensively. Zhang et al. (2010) focused on interannual sea ice variations in the Bering Sea, which they found to be dominated by wind-driven changes in ice transport and the ocean thermal front in the southern Bering Sea. From a large-scale perspective, the interannual variability of sea ice in the Bering Sea is mainly driven by atmospheric forcing, especially in winter (Walsh and Johnson 1979; Walsh and Sater 1981; Niebauer 1980, 1983, 1988, 1998; Niebauer and Day 1989; Rogers 1981; Overland and Pease 1982; Sasaki and Minobe 2005). The winter atmospheric conditions over the Bering Sea (surface air temperature and winds) and the Bering Sea ice cover are mainly determined by the position of the Aleutian Low (Rogers 1981; Cavalieri and Parkinson 1987; Niebauer 1998; Rodionov et al. 2005, 2007). The winter air temperature and sea ice extent are also related to storm track changes associated with the strength of the Aleutian Low (Overland and Pease 1982; Rodionov et al. 2007). Additionally, the local wind variability, which is associated with geopotential height anomalies over Alaska and temperature anomalies over the northern Bering Sea, is also important (Sasaki and Minobe 2005). On larger scales, the ice concentration anomalies in the Bering Sea and the Sea of Okhotsk tend to be opposite, and they are believed to result from atmosphere circulation variations 1 month

earlier (Niebauer 1983; Cavalieri and Parkinson 1987; Fang and Wallace 1994; Deser et al. 2000). Furthermore, the Bering Sea experiences atmospheric teleconnections from El Niño/Southern Oscillation (ENSO), the Pacific North-American (PNA) pattern (Niebauer 1980, 1988, 1998; Niebauer and Day 1989, Overland et al. 1999), the Arctic Oscillation (e.g., Overland et al. 1999), the North Pacific Oscillation (NPO)/Western Pacific (WP) pattern (Rogers 1981; Fang and Wallace 1994; Linkin and Nigam 2008; Matthewman and Magnusdottir 2011), the East Asia-North Pacific winter climate (Liu et al. 2007), and the East Asian summer monsoon (Zhao et al. 2004).

Here, we address the driving mechanisms of sea ice anomalies from the mean seasonal cycle in the Bering Sea, and we quantify the relative roles of thermodynamic and dynamic processes during 1980–1989. We use a high-resolution (nominally 0.1°) global coupled ocean sea-ice model forced with interannually varying atmospheric reanalysis fields. We partition the ice volume change into thermodynamic and dynamic components, and we investigate the relationship between ice variability and atmospheric and oceanic conditions. The results yield a depiction of the physical processes driving sea ice variability in the Bering Sea as revealed by a high-resolution ice-ocean model. The results illustrate the importance of thermodynamic processes on the large scale and dynamic processes locally near the ice margins. Thermodynamic ice volume change is controlled by surface heat exchange with the atmosphere in most of the Bering Sea and by ice-ocean heat fluxes near the ice edge in the south. Ice motion is generally consistent with wind stress acting as the driving agent, except near certain straits in the north.

Section 2 describes the ice-ocean model. Section 3 presents the results, which focus on the relationships between sea ice variability in the Bering Sea and external forcing, treating thermodynamic and dynamic processes separately. Section 4 contains a discussion of the results, and Sect. 5 provides the conclusions.

2 Methods

We use output from a fine resolution (nominally 1/10°) global coupled ocean/sea-ice model configured in the Community Earth System Model (CESM) framework (McClean et al. 2014, in preparation). The ocean and sea ice components are the Los Alamos National Laboratory Parallel Ocean Program (POP) and the Los Alamos Sea Ice Model (CICE); POP and CICE are coupled in CESM via Flux Coupler version 7 (CPL7) (Craig et al. 2012). This model uses a tripole grid with poles in Canada, Russia, and Antarctica. Details of the global ocean bathymetry for this tripole grid are found in McClean et al. (2011). Figure 1 shows the ocean model
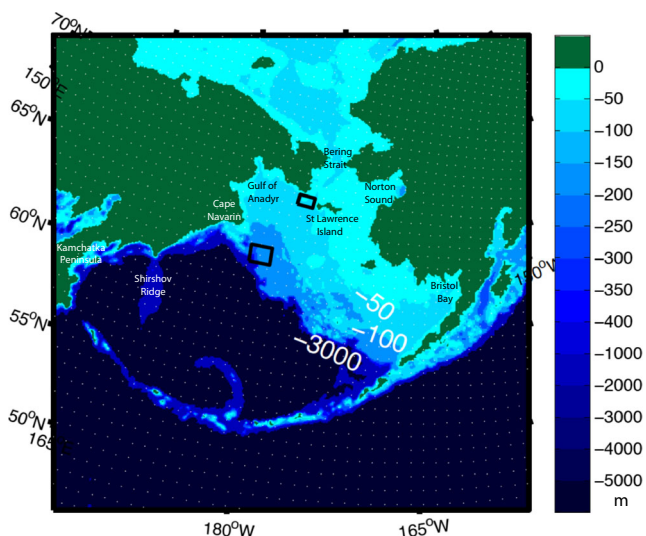
Fig. 1 Ocean model bathymetry of the Bering Sea. *White dots* indicate the model temperature grid subsampled every ten points. Two *black boxes* indicate the two key sites chosen for studying local forcing of ice variations in Sect. 3.2

bathymetry of the Bering Sea, as well as the model grid subsampled at every tenth grid point.

CICE utilizes the energy-conserving thermodynamic sea ice model of Bitz and Lipscomb (1999) to compute ice/snow growth and melt rates. CICE has one snow thermodynamic layer and four ice thermodynamic layers. CICE uses a subgridscale ice thickness distribution with five ice thickness categories: 0.00–0.60, 0.60–1.40, 1.40–2.40, 2.40–3.60, and >3.60 m. For each ice thickness category, the model calculates the ice and snow thickness changes and vertical temperature profiles based on vertical radiative, turbulent, and conductive heat fluxes. The model includes the effect of brine pockets on effective specific heat capacity and thermal conductivity due to internal melting and freezing. The salinity is prescribed to follow a vertical profile that is constant in time. CICE uses the elastic-viscous-plastic (EVP) sea ice dynamic model of Hunke and Dukowicz (1997) to compute ice velocities. The ice momentum equation involves five terms: wind stress, ocean stress, divergence of the internal ice stress tensor, the Coriolis force, and gravitational force due to the sea surface slope. CICE uses an incremental remapping advection scheme to transport sea ice in various thickness categories (Lipscomb and Hunke 2004).

POP is a *z*-level ocean general circulation model that solves the three-dimensional primitive equations for ocean temperature, salinity, and momentum (Dukowicz and Smith 1994). It has an implicit free surface. It uses partial bottom cells for improved representation of flow over the bottom boundary. This POP configuration has 42 vertical levels whose thickness ranges from 10 m in the uppermost level to 250 m in the deep ocean. The horizontal resolution is around 6 km in the Bering Sea.

This ocean/sea ice simulation was forced with Coordinated Ocean-ice Reference Experiment version 2 (CORE2) interannually varying atmospheric forcing from 1970 to 1989 (Large and Yeager 2004, 2009). CORE2 fluxes are based upon six hourly (1948–2006) near-surface vector wind, specific humidity, density, and air temperature based on National Center for Environmental Prediction (NCEP) reanalysis; daily downward radiation (1984–2006) from International Satellite Cloud Climatology Project (ISCCP) data (Zhang et al. 2004); and monthly precipitation (1979–2006) from a combination of satellite observations. Climatological mean annual cycles are used for all radiation fluxes (1948–1983) and precipitation (1948–1978) before the satellite observing periods. Some data sets are adjusted using observations. Over the Arctic cap north of 70° N, 12 monthly adjustments are made to the surface air temperature based on the polar exchange at the sea surface (POLES) data (Rigor et al. 2000). Adjustments are also made to the NCEP vector winds using QSCAT satellite scatterometer wind vectors. Turbulent fluxes are obtained using bulk formulae, the near surface NCEP atmospheric state, and upper-level model temperature and velocity (Large and Yeager 2004, 2009; Griffies et al. 2009; Griffies et al. 2012). CORE2 is on a T62 grid with a horizontal resolution of ~100 km (east-west) and ~200 km (north-south) in the Bering Sea. This CORE2 forcing data set was also used by Danielson et al. (2011) to drive Bering Sea simulations with the Regional Ocean Modeling System (Haidvogel et al. 2008). Weak surface salinity restoring with an effective timescale of about 4 years was used in this simulation to limit model drift.

This version of POP uses the K-Profile Parameterization (KPP) for vertical mixing. It does not include tidal forcing. Earlier numerical studies have found that tidal forcing increases vertical mixing and the kinetic energy of ocean currents in the southeastern Bering Sea (Hermann et al. 2002), as well as modifying sea ice thickness in the central-eastern Bering Sea (Zhang et al. 2010). Tidal forcing might also reduce the mean flow due to the horizontal gradient of tidal mixing (Auad and Miller 2008).

The model calculates thermodynamic and dynamic ice volume tendencies as diagnostics, which are saved as monthly averages during the model integration. We investigate the variability of ice and atmosphere/ocean conditions from 1980 to 1989; model outputs from 1970 to 1989 were available at the time of the analysis, and the first 10 years (1970–1979) were treated as the spin-up period. We focus on anomalies from the mean seasonal cycle, which is computed for the period 1980–1989.

We use satellite passive microwave observations of sea ice concentration on a ~25-km grid for model validation. The observations are the Bootstrap Sea Ice Concentrations from Nimbus-7 SMMR and DMSP SSM/I-SSMIS, which is publicly available from the National Snow and Ice Data Center (Comiso 2000).

3 Results

3.1 Variability of sea ice and climatic forcing over the entire ice cover of the Bering Sea

Here, we consider the entire sea ice cover in the Bering Sea. Focused analyses of two locations are discussed below in Sect. 3.2.

3.1.1 Sea ice mass budget over the entire ice cover of the Bering Sea

The modeled total ice area in the Bering Sea (the sum of ice concentration multiplied by the grid cell area for grid cells where ice concentration is at least 15 %), averaged for each month from 1980 to 1989, is shown in Fig. 2; ice area anomalies from the mean seasonal cycle are also included. The model results are compared with ice area calculated from satellite observations of sea ice concentration (fractional ice cover in each grid cell). The model captures much of the observed ice area variability, with the correlation coefficient between modeled and observed anomalies being 0.95. Although the model underestimates ice area during winter months (Fig. 2a), the amplitude of the winter anomalies matches the observations relatively well (Fig. 2b).

As shown in Fig. 3a, b, the simulated total ice volume in the Bering Sea for 1980–1989 displays substantial interannual variability. The lowest ice volume winter maxima occur in 1982 and 1989 ($\sim 3.2 \times 10^{11}$ m^3), and the highest winter maxima occur in 1984 and 1988 ($\sim 5.4 \times 10^{11}$ m^3). Opposite extremes can occur in consecutive years, e.g., in 1988 and 1989. The time series of ice volume anomalies (with monthly climatology subtracted) shows that the largest anomalies are

concentrated in winter and spring when the ice volume is large and that they can occur in different months during these seasons. The largest negative anomaly occurs in February 1985, and the largest positive anomaly occurs in March 1984. We note that the timing of ice growth is important. Usually, early ice growth leads to a lower winter maximum later, e.g., in the winter of 1989, while late ice growth leads to a larger winter maximum, e.g., in the winters of 1984 and 1985. This produces winter dipole structures in the time series of the ice volume anomalies.

In Fig. 4, we consider the ice volume tendency (time derivative of ice volume), which is related to atmospheric and oceanic forcings. We partition the ice volume change into thermodynamic and dynamic components. The thermodynamic ice volume tendency is the sum of the thermodynamic ice growth rate (including congelation ice growth, frazil ice growth, and snow ice formation) and the thermodynamic ice melt rate (including ice melt at the bottom, surface, and lateral sides of sea ice), where a positive/negative value means ice volume increase/decrease due to thermodynamic processes. The dynamic ice volume tendency is the ice volume change due to ice motion, where a positive/negative value means ice volume increase/decrease resulting from net ice volume transport into/out of a certain region. The net ice volume tendency is the sum of the thermodynamic ice volume tendency and the dynamic ice volume tendency.

Thermodynamic and dynamic ice volume tendencies integrated over the entire Bering Sea reveal the relative importance of freezing/melting and ice transport through the boundary (i.e., through the Bering Strait) on the total ice volume change in the Bering Sea. The net, thermodynamic, and dynamic ice volume tendencies summed over the ice-covered area for the whole Bering Sea, as well as their anomalies, are calculated for each

Fig. 2 **a** Total ice area in the Bering Sea from the model (*blue*) and from satellite passive microwave observations (*red*). **b** Anomalies from the 1980–1989 mean seasonal cycle of ice area from the model (*blue*) and from observations (*red*)
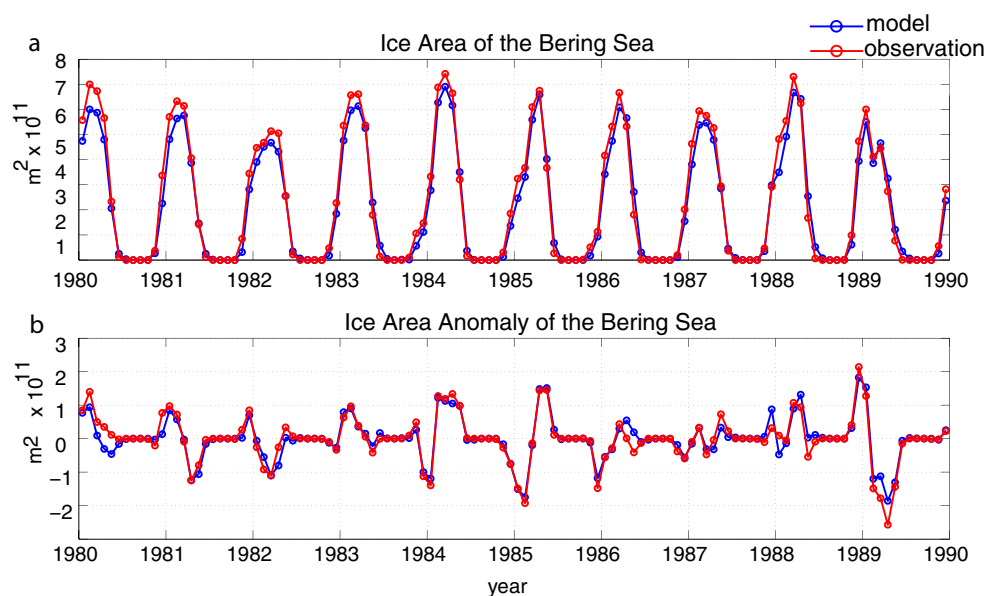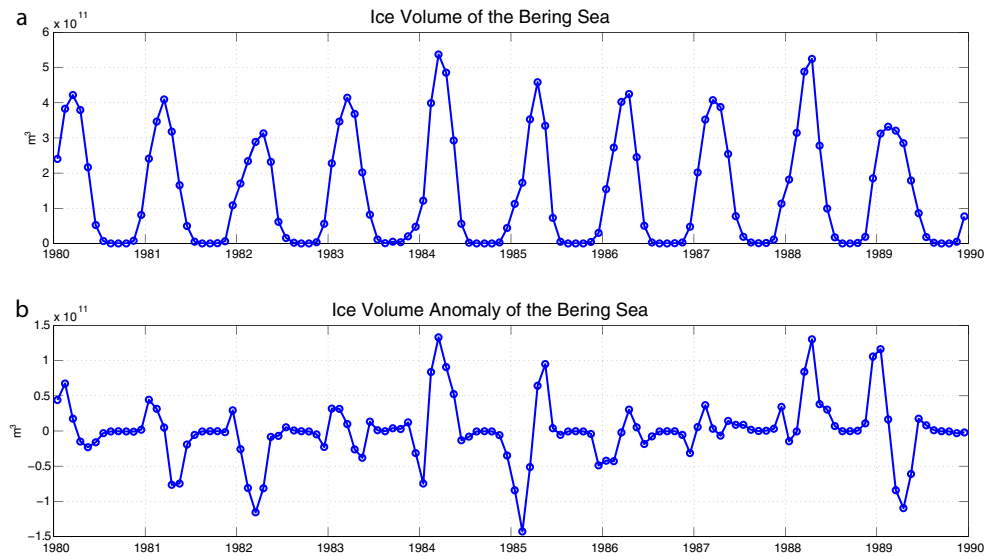
Fig. 3 a Modeled total ice
volume in the Bering Sea. **b**
Anomaly from the mean seasonal
cycle of total ice volume in the
Bering Sea

month during 1980–1989. As shown in Fig. 4a, the net ice
volume tendency is typically dominated by the thermodynamic
ice volume tendency, and the contribution of ice dynamics is
relatively small except for some key anomaly events. For example,
in February 1989, the dynamic tendency is 3.5 times as large
as the thermodynamic tendency but with an opposite sign,
implying that the net ice volume change is primarily related to
ice dynamics. Though the dynamic contribution over the whole
Bering Sea is usually small, the local dynamic tendency can be
very large (see Sect. 3.2.1), with a dipole-like pattern in the
spatial distribution (Li et al. 2014).

In terms of anomalies from the mean seasonal cycle, net ice
volume change is more consistent with thermodynamics in
general, but dynamics are important in some cases such as in
February 1989 (Fig. 4b). Dynamic anomalies are generally

somewhat weaker in magnitude than thermodynamic anomalies,
but they can be stronger such as in February 1989. Dynamic and
thermodynamic anomalies usually have opposing signs, but in
some large anomaly events such as in February 1984 and February
1989, the two components occur with the same sign,
producing extreme net tendency anomalies.

The ice volume tendencies have large variations from year
to year, especially in winter and spring when ice is abundant.
In February 1984, thermodynamic, dynamic, and net ice volume
tendency anomalies all reached their most positive values
during 1980–1989. In February 1989, anomalies of net and
dynamic ice volume tendencies all reached their most negative
values, and the thermodynamic tendency anomaly is also very
negative. Detailed examinations of these two large anomaly
events are presented below in Sect. 3.3.

Fig. 4 a Thermodynamic (*red*),
dynamic (*blue*), and net (*black*)
ice volume tendencies integrated
over the entire Bering Sea. **b**
Anomalies of thermodynamic
(*red*), dynamic (*blue*), and net
(*black*) ice volume tendencies
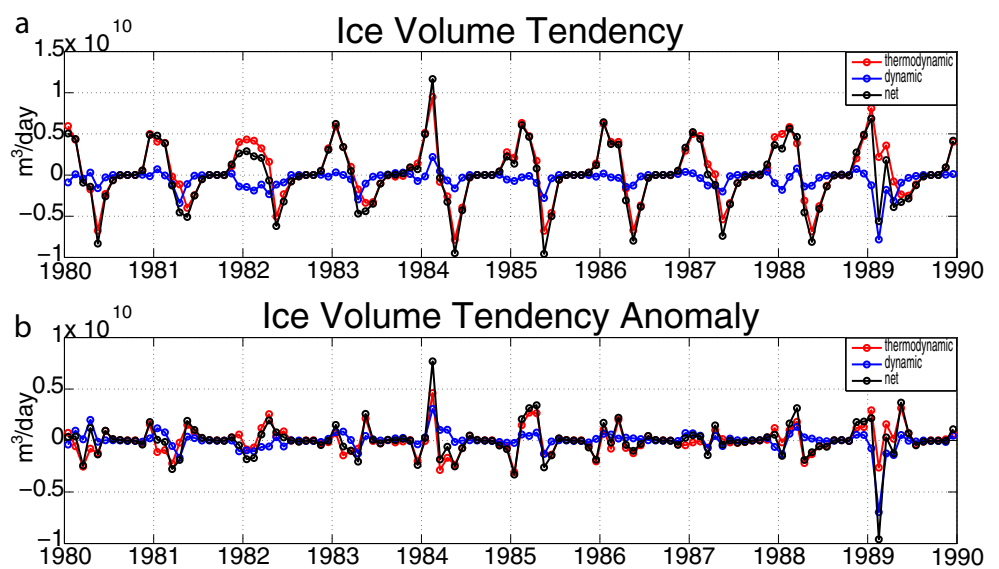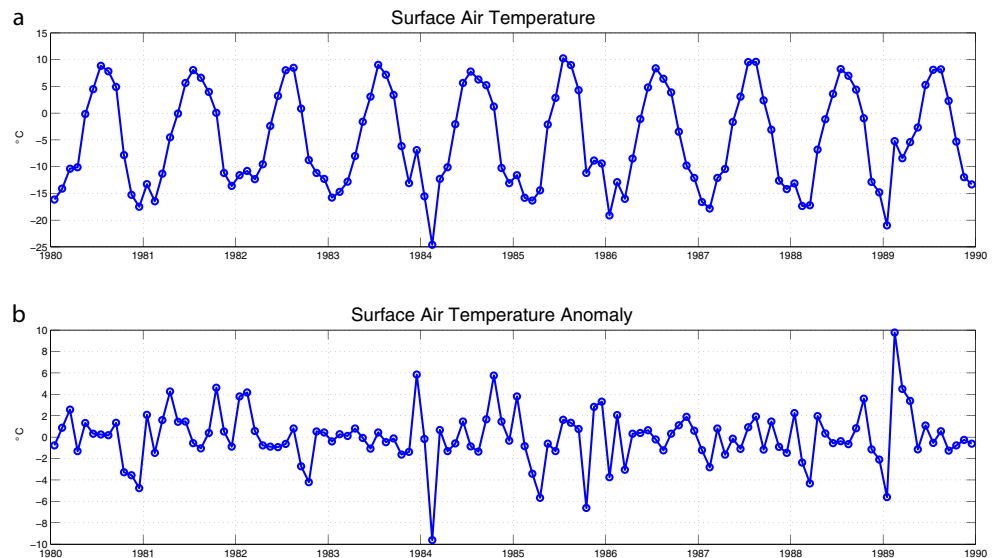integrated over the entire Bering
Sea

3.1.2 Sea ice heat budget over the entire ice cover of the Bering Sea

As shown in the previous section, the net ice volume tendency for the whole Bering Sea is dominated by the thermodynamic ice volume tendency. Here, we show that the winter thermodynamic ice volume tendency is mainly controlled by the net surface energy flux (between the ice and the atmosphere) and surface air temperature. The surface air temperature and net surface energy flux are averaged over the ice-covered area in the Bering Sea, and then their anomalies are calculated, as shown in Figs. 5 and 6. Surface air temperature and surface energy flux anomalies have high correlations with

thermodynamic ice volume tendency anomaly in winter, with correlations of −0.74 and −0.68, respectively, at zero lag.

The surface air temperature changes rapidly and has large variations, as shown in Fig. 5. The coldest February air temperature (∼−25 °C) occurring in 1984 and the warmest February air temperature (∼−5 °C) occurring in 1989 correspond to the two largest ice volume tendency anomalies (with opposite signs) in Fig. 4b. This suggests that surface air temperature strongly controls ice volume tendency.

We further partition the net surface energy flux into its four components: net shortwave radiation, net longwave radiation, latent heat flux, and sensible heat flux (Fig. 6a). For the net shortwave radiation, we take the incoming solar radiation
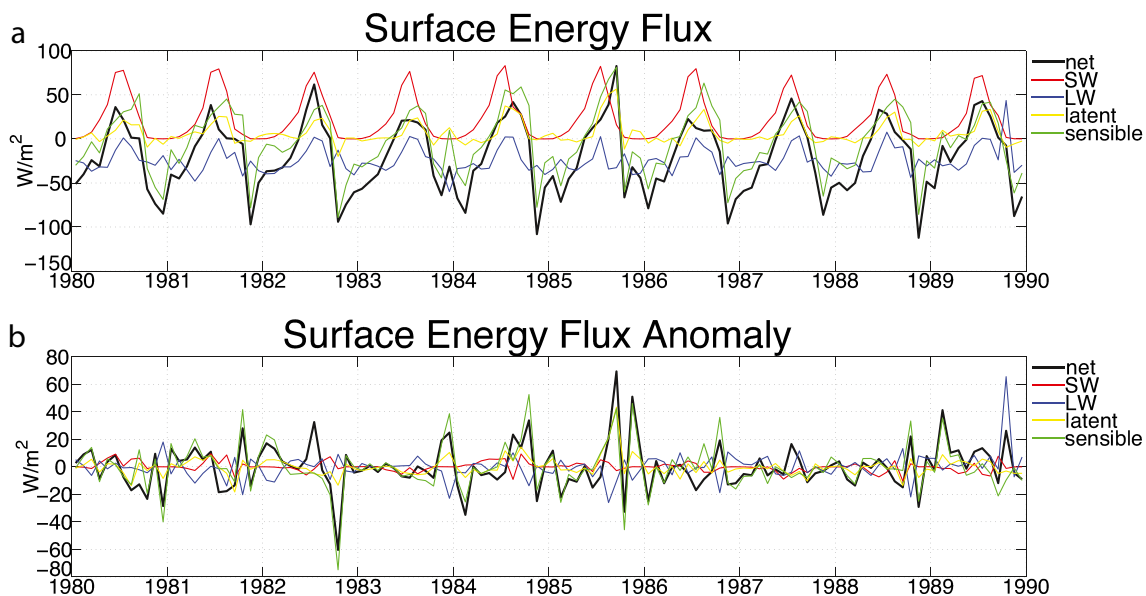

Fig. 6 **a** Net surface energy flux (*black*), net shortwave radiation (*red*), net longwave radiation (*blue*), latent heat flux (*yellow*), and sensible heat flux (*green*), averaged over the ice-covered area of the Bering Sea. **b** Anomalies of net surface energy flux (*black*), net shortwave radiation (*red*), net longwave radiation (*blue*), latent heat flux (*yellow*), and sensible heat flux (*green*), averaged over the ice-covered area of the Bering Sea

minus the reflected solar radiation and subtract the small amount of solar radiation that penetrates into the ocean below the ice. The net longwave radiation is the sum of the incoming longwave radiation, which is specified in the atmospheric forcing, and the outgoing longwave radiation, which is calculated based on the ice/snow surface temperature.

In Fig. 6a, the sensible heat flux visually corresponds closely with net surface energy flux. During the fall and winter seasons, sensible heat flux and net longwave radiation dominate the net surface energy flux, while net shortwave radiation and latent heat flux are relatively small. In spring, high values of shortwave radiation nearly balance longwave radiation while sensible and latent heat fluxes are small. The net solar radiation varies little from year to year. As shown in Fig. 6b, the interannual variability of net surface energy flux is dominated by sensible heat flux, with a correlation coefficient of 0.83. Latent heat flux anomalies also correlate well with net surface energy flux anomalies, having a correlation of 0.71, but with very small relative magnitude. Longwave radiation variations generally oppose net surface energy flux variations, acting as a negative feedback. Sensible heat flux, latent heat flux, and outgoing longwave radiation are all computed interactively in the model based on the surface temperature of snow-free ice or snow, so that net surface energy flux should have a close relationship with surface air temperature. In fact, the net surface energy flux variation has a 0.60 correlation with surface air temperature variation, including all months, which increases to 0.88 when considering only winter months.

The main results of the surface energy flux budget analysis for Bering Sea ice cover are summarized as follows:

1. Sensible heat flux dominates the net surface energy flux.
2. Longwave radiation is typically second largest term.
3. Shortwave radiation is relatively small in fall and winter when ice grows and reaches its maximum but is larger during spring ice retreat.
4. Latent heat flux has the smallest magnitude among the surface energy flux components, but it correlates closely with net surface energy flux.
5. The net surface energy flux variability can be largely explained by the surface air temperature anomaly (which is specified from observations), especially in winter.

The high correlation found between modeled and observed ice area in this simulation (and that of Danielson et al. 2011) therefore appears to be largely due to the specified surface air temperature anomalies, which are closely correlated with observed ice cover anomalies. This may also help account for the simulated agreement with ice cover observations despite tidal forcing not being included in this simulation as a driving process for mixing and current rectification in the shallow waters of the Bering Sea (Hermann et al. 2002; Zhang et al. 2010).

3.1.3 Sea ice force balance over the entire ice cover of the Bering Sea

In this section, the force balance per unit area of the sea ice pack is analyzed. The vertically integrated, two-dimensional momentum equation for sea ice involves five terms: wind stress ($\overrightarrow{\tau}_a$), ocean stress ($\overrightarrow{\tau}_w$), divergence of the internal ice stress tensor ($\nabla \cdot \sigma$), the Coriolis body force ($-\widehat{k} \times mf\overrightarrow{u}$), and the gravitational force due to sea surface slope ($-mg\nabla H_0$, with sea surface height H_0 relative to the geoid):

$$m\frac{\partial \overrightarrow{u}}{\partial t} = \overrightarrow{\tau}_a + \overrightarrow{\tau}_w + \nabla \cdot \sigma - \widehat{k} \times mf\overrightarrow{u} - mg\nabla H_0$$

where m is the combined mass of ice and snow per unit area.

Monthly mean wind stress on the ice, ocean stress on the ice, divergence of the internal ice stress tensor, and Coriolis force are archived in the model output. We construct the gravitational force due to sea surface slope based on model outputs of sea surface height, ice thickness, and snow thickness.

We construct time series of ice velocity, wind stress, ocean stress, the Coriolis force, divergence of the internal ice stress tensor, the gravitational force due to sea surface slope, and net force averaged over the ice-covered area, as well as time series of their anomalies after removing the mean seasonal cycle (Fig. 7). The ice velocity correlates with simultaneous wind stress, especially in the meridional direction (compare Fig. 7c and the red curve in Fig. 7a, also compare Fig. 7i and the red curve in Fig. 7g). As shown in Fig. 7a, b, wind stress is the largest term, and the oppositely directed ocean stress is slightly weaker. The divergence of the internal ice stress is usually the third largest term, in the opposite direction to the wind stress, and can be as large as the ocean stress in the meridional direction, such as during the February 1989 anomaly event. The divergence of the internal ice stress plays a larger role in the zonal direction than in the meridional direction. This is expected to be due to the geometry of the Bering Sea, in that the Bering Sea is bounded by land in the east-west direction, and in the south, it is open ocean. Ice typically moves southwestward (Fig. 7c, d). Thus, ice has more compression near the western land boundary and moves more freely to the south. It should be noted that this is the spatial average of the divergence of the internal ice stress, which is quite inhomogeneous in space. So, the actual values near the key land boundaries are even larger than this mean value, and the values are small over the central and southern ice-covered region. The Coriolis force and the gravitational force due to sea surface slope are typically small. The net of these five forces is nearly zero, indicating force equilibrium where ice
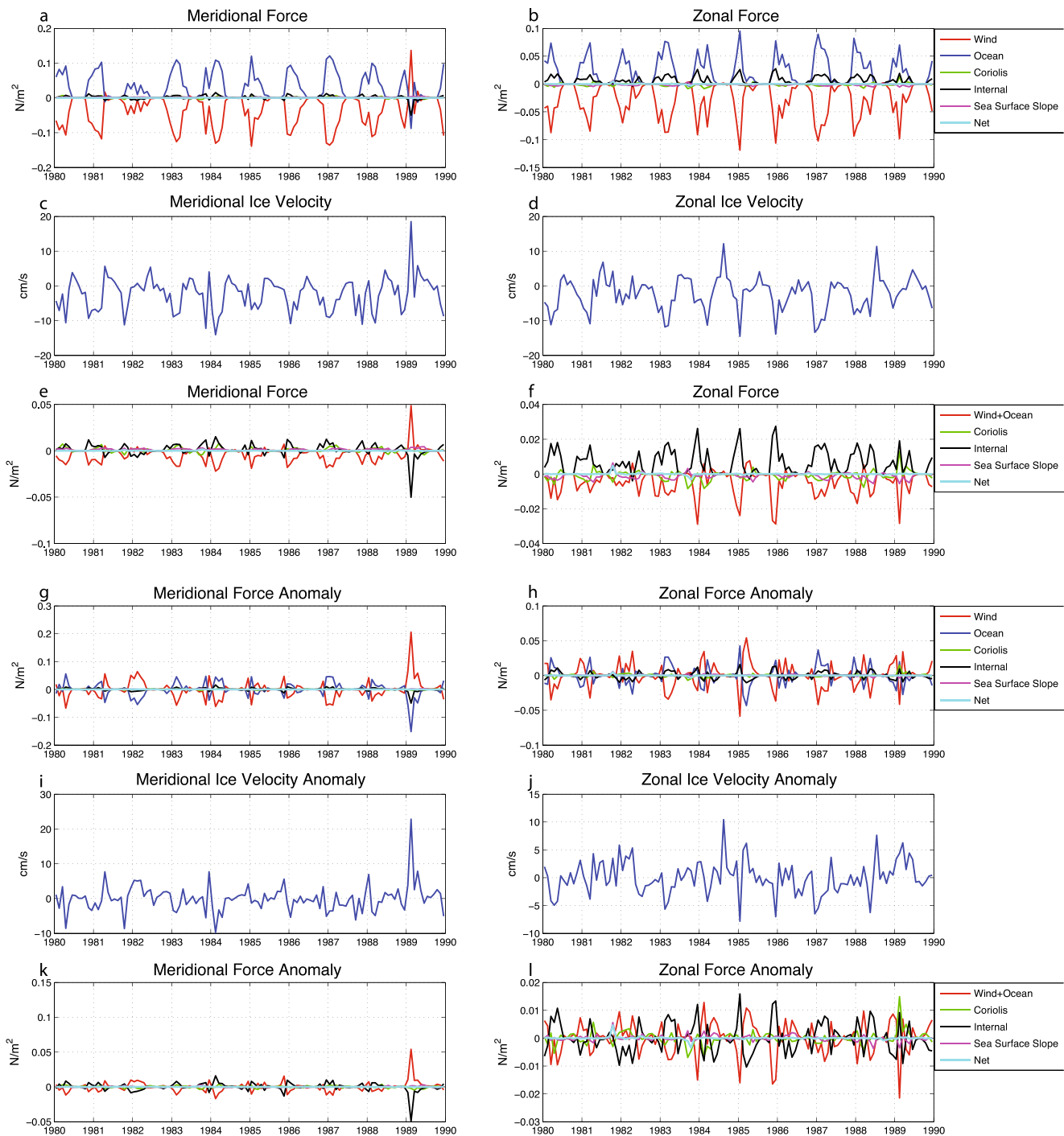
Fig. 7 **a** Meridional components averaged over the ice-covered area of the Bering Sea of wind stress on ice (*red*), ocean stress on ice (*blue*), Coriolis force (*green*), divergence of the internal ice stress (*black*), gravitational force due to sea surface slope (*magenta*), and net force (*cyan*). **b** As in **a** but for zonal components. **c** Meridional ice velocity averaged over the ice-covered area of the Bering Sea. **d** Zonal ice velocity averaged over the ice-covered area of the Bering Sea. **e** Meridional components averaged over the ice-covered area of the Bering Sea of the sum of wind stress and ocean stress (*red*), Coriolis force (*green*), divergence of the internal

ice stress (*black*), gravitational force due to sea surface slope (*magenta*), and net force (*cyan*). **f** As in **e** but for zonal components. **g** As in **a** but for anomalies from the mean seasonal cycle. **h** As in **g** but for zonal components. **i** Anomalies form the mean seasonal cycle of meridional ice velocity averaged over the ice-covered area of the Bering Sea. **j** Anomalies from the mean seasonal cycle of zonal ice velocity averaged over the ice-covered area of the Bering Sea. **k** As in **e** but for anomalies from the mean seasonal cycle. **l** As in **k** but for zonal components

acceleration is relatively small on the monthly mean timescale.

Since the largest two stresses (wind and ocean) are nearly counterbalancing each other, it is useful to examine the residual sum of these two terms in relation to the other (smaller) terms in the force balance. In Fig. 7e, f, we compare this residual sum to the Coriolis force, divergence of the internal ice stress tensor, and gravitational force due to sea surface slope averaged over the ice-covered area, as well as anomalies of these quantities from the mean seasonal cycle (Fig. 7k, l). The residual sum is usually in the same direction as the wind, implying wind-driven ice flow with opposing ocean drag. Divergence of the internal ice stress also opposes the residual sum, resisting ice motion. The smallest terms, Coriolis force and gravitational force due to sea surface slope, have similar magnitudes to each other.

Our results are consistent with previous work in the Arctic Ocean by Steele et al. (1997). They show that the Coriolis force and gravitational force due to sea surface slope are relatively small and that the largest terms are wind stress, ocean stress, and divergence of the internal ice stress.

Our results imply that Bering Sea ice motion is largely driven by wind stress, especially along the ice edge where sea ice is close to a freely drifting state. This is consistent with other studies (Thorndike and Colony 1982; Reynolds et al. 1985; Kimura and Wakatsuchi 2000, 2001). Thorndike and Colony (1982) showed that the wind (estimated geostrophically from sea level pressure) explains a large fraction of the variance of ice velocity in the central Arctic on short timescales, while the long-term (several month) averaged ice motion has equal contributions from the geostrophic wind and the mean ocean circulation. Reynolds et al. (1985) show that in the open ocean, sea ice moves to the right of surface wind at an angle of 30° at approximate 4 % of the wind speed at 3 m. Kimura and Wakatsuchi (2000, 2001) show a high correlation of sea ice motion and wind along the ice edge in the Bering Sea on daily timescales.

Here, we can also evaluate the free drift assumption for Bering Sea ice motion away from land (Pease and Overland 1984; Reynolds et al. 1985; Connolley et al. 2004). We ignore the ice acceleration term in the force balance since it was found above to be small. We can also ignore the gravitational force due to sea surface slope without much loss of accuracy, except in certain northern coastal regions. However, the divergence of the internal ice stress is only small in the central and southern ice-covered area; it can be large at some local spots near the land boundaries in the north. Although these previous studies retain the Coriolis force, we find here that this term is very small, and it is only relatively important near the ice edge. Therefore, free drift of sea ice neglecting Coriolis is a reasonably accurate approximation in the central and southern ice-covered area in the Bering Sea but is less valid in the northern regions near land.

3.2 Local forcing of sea ice variations in the Bering Sea

Integrating the characteristics of ice over the entire basin can mask the local importance of various terms in the balances. Some terms may have spatial averages that are small even though they exhibit large-scale structures, which are regionally important. To better understand the relationship between ice variables and environmental conditions, we focus on two key locations in the Bering Sea (Fig. 1), one in the northern "growth" region (a 90 km by 60 km box centered at 63.76° N, 173.01° W) and one in the southern "melt" region (a 127 km by 100 km box centered at 60.89° N, 178.31° W). These two localities are examples of the large growth rate near the northern coastal polynyas and the large melt rate near the southern ice edge, under the additional influence of strong advective affects.

3.2.1 Local ice mass budget

When considering the local climate forcing of ice variability, it is useful to separate thermodynamic and dynamic ice volume tendencies, which exhibit large interannual variability while the net ice volume tendency remains relatively stable. The separation of thermodynamic and dynamic processes can differentiate ice responses to thermal and mechanical forcings.

We calculate the spatial mean of the thermodynamic, dynamic, and net ice volume tendencies for a box in the north and a box in the south separately. We adopt the sign convention that positive thermodynamic tendency is ice growth and negative thermodynamic tendency is ice melt.

At the northern site (Fig. 8), the thermodynamic processes mainly cause ice growth (Fig. 8b), and ice is transported out of this region in winter (blue curve in Fig. 8a). During fall and spring, when the ice edge passes through this site, ice melt occurs (Fig. 8b), but here, we focus on the winter season. When the external disturbance is large enough, the ice response is substantial. In the warm winters of 1982 and 1989, both the thermodynamic ice growth and the dynamic ice transport out of the region are weak (Fig. 8a). In contrast, in the cold winters of 1983 and 1984, ice growth and ice advection are strong (Fig. 8a). These anomaly events can be explained by the atmospheric forcing. As shown in Fig. 9a, b, in the winters of 1982 and 1989, the surface air temperature is warmer than normal (Fig. 9b), the surface energy fluxes are weaker (Fig. 9a), and consequently, the ice growth is suppressed (Fig. 8b). Additionally, prominent anomalous southerly winds (Fig. 9c, d) reduce the ice transport out of this region (Fig. 8a). In contrast, in the winters of 1983 and 1984, colder air temperature (Fig. 9b), stronger surface energy flux (Fig. 9a), and stronger northerly winds (Fig. 9c, d) produce more ice growth and more ice transport (Fig. 8a).

Next, we quantify how ice variables and processes are related to environmental conditions at this location. Surface energy flux
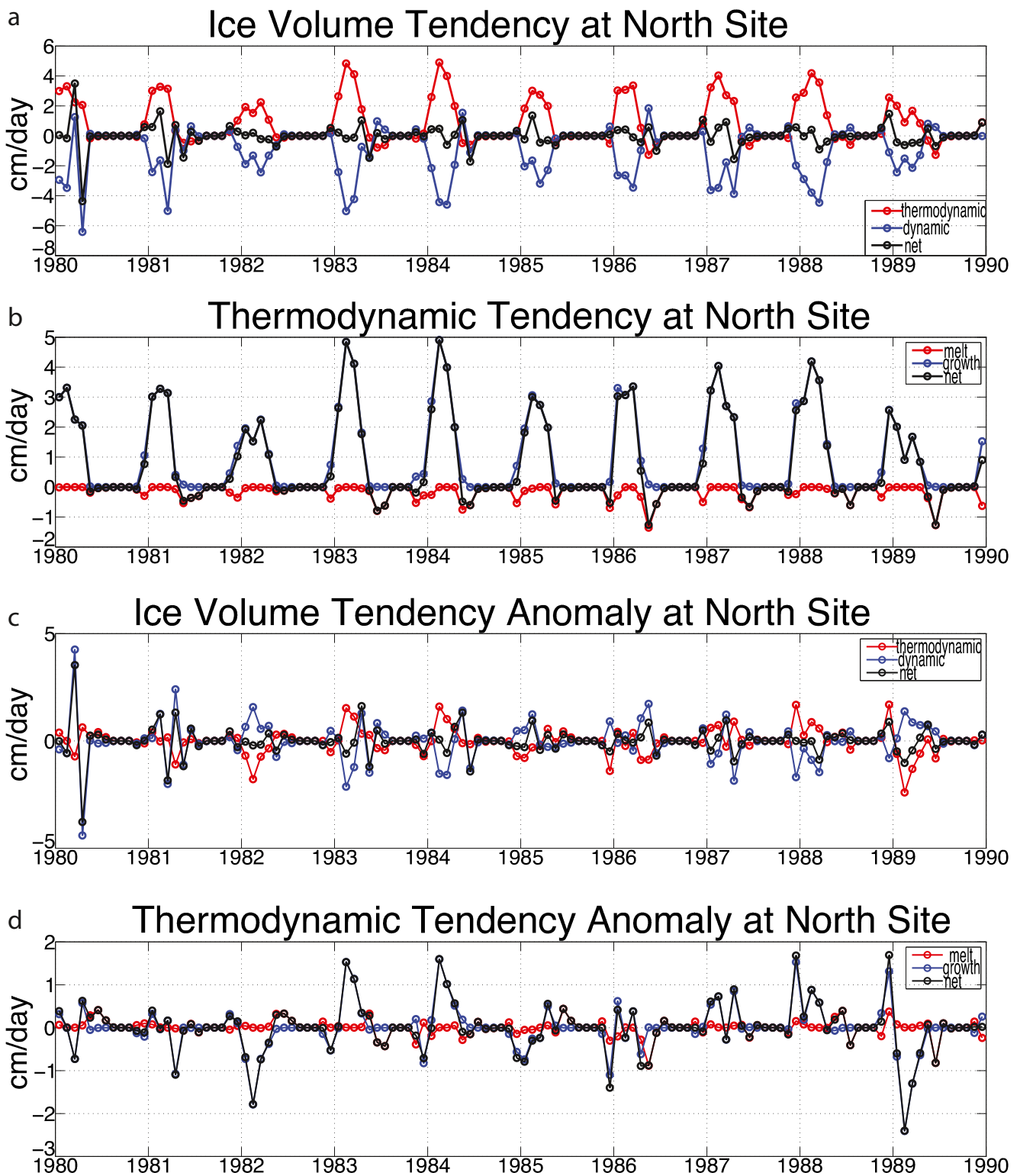
Fig. 8 **a** Thermodynamic (*red*), dynamic (*blue*), and net (*black*) ice volume tendencies averaged over the northern box in Fig. 1. **b** Thermodynamic ice melt rate (*red*), thermodynamic ice growth rate (*blue*), and net thermodynamic tendency (*black*) at northern site. **c** Anomalies of thermodynamic (*red*), dynamic (*blue*), and net (*black*) ice volume tendencies at northern site. **d** Anomalies of ice melt rate (*red*), ice growth rate (*blue*), and net thermodynamic tendency (*black*) at northern site. In each panel, volumes are normalized by the area of the *box*, giving units of thickness (cm)

Fig. 9 **a** Surface energy flux anomaly, **b** surface air temperature anomaly, **c** meridional wind anomaly, and **d** zonal wind anomaly averaged over the northern box in Fig. 1

and surface air temperature (Fig. 9a, b) correspond closely with thermodynamic ice volume changes (Fig. 8a, c). The correlation between surface energy flux anomalies and thermodynamic tendency anomalies considering all months is high (−0.92), and it is even higher when considering only winter months (−0.98). This agrees with expectations: Neglecting sensible heat storage in the ice and ice-ocean heat fluxes, the surface energy flux should be equal to the change in latent heat of the ice, which is proportional to ice volume. The correlation between surface air temperature anomaly and thermodynamic tendency anomaly is lower than this, −0.68 for all months and −0.73 for winter. This implies that surface air temperature does not wholly determine the surface energy flux and hence ice growth in this region, although it has a substantial effect.

The ice transport out of the northern region (Fig. 8a, c) is suppressed by southerly wind anomalies and promoted by northerly wind anomalies (Fig. 9c, d). Wind stress largely drives the ice motion. This is evident in the high correlation, 0.89, between the meridional ice velocity and meridional wind stress (not shown here).

At the northern site, the anomalies of thermodynamic and dynamic ice volume tendencies are opposite in sign with similar magnitudes and a correlation coefficient of −0.67, as shown in Fig. 8c. These two effects nearly balance each other, leaving a small residual. The small residual tends to be dominated by the dynamic term. This is indicative of there being a relatively stable ice cover here in winter, with changes caused by wind forcing being nearly compensated by thermodynamic

effects. However, an exception to this generalization is the large anomaly event of winter 1989 when the net ice volume tendency is dominated by thermodynamic effects. In that event, warm air (Fig. 9b) contributes to lower ice growth, while southerly winds (Fig. 9c) advect thick ice into the region, restoring toward more typical conditions.

The southern site (Fig. 10) is near the ice edge in winter. Ice volume tendencies here are dominated by dynamic ice transport into the region and ice bottom melt in winter (very weak ice growth also occurs in winter) (Fig. 10a, b). During the winters of 1982 and 1989 when the wind is southerly (Fig. 11c), both ice transport from the north and local basal melting are reduced (Fig. 10a) because anomalous southerly winds cause anomalous northward ice velocity and less ice is left for melting at this local site. During the winters when stronger northerly winds blow such as in 1980, 1983, and 1987 (Fig. 11c), both ice transport into this site and basal melting increase (Fig. 10a).

Since this site is close to the southwestern ice edge, ice dynamical effects in winter are significant (Fig. 10a) due to a substantial spatial gradient in ice thickness and large winds in the area. The ice response to atmospheric thermal forcing (Fig. 11a, b) is evident, but not as strong as in the northern site. The correlation of the surface air temperature anomaly with the thermodynamic ice volume tendency anomaly is 0.51 (0.60 in winter), which is not as high as in the northern site. Because near the southwestern ice edge the thermodynamic effect is dominated by ice bottom melting from warm ocean water, the thermodynamic ice volume tendency would be
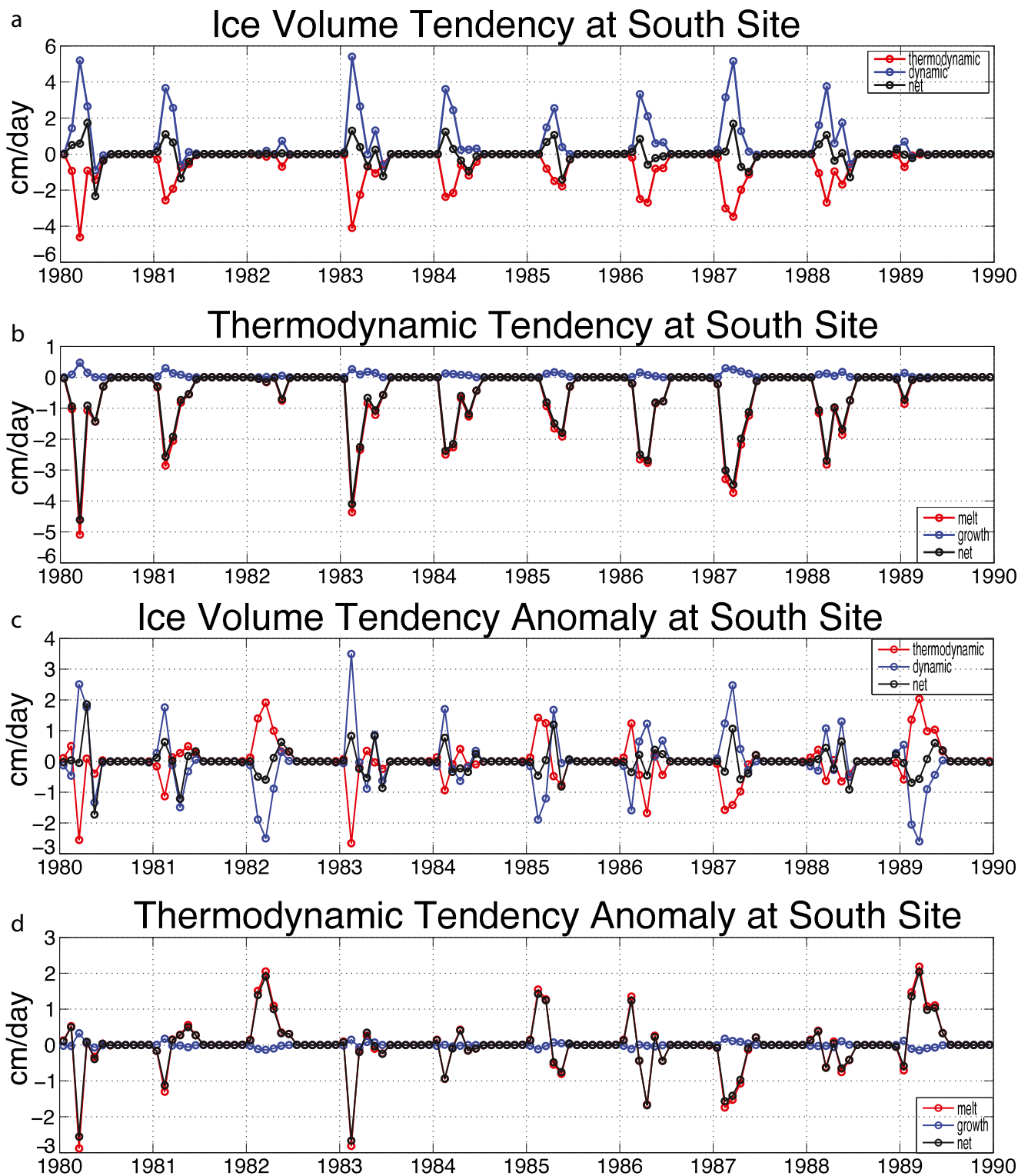
Fig. 10 As in Fig. 8 but for the southern box in Fig. 1

expected to be associated more with oceanic forcing (Fig. 12a). Indeed, the oceanic heat flux anomaly (Fig. 12a) and thermodynamic tendency anomaly (red curve in Fig. 10c) have a high correlation, 0.99, suggesting that oceanic heat flux controls ice melting near the ice edge. Note also that positive

ocean zonal velocity anomalies occur before the positive sea surface temperature anomalies in the 1982 and 1989 low ice years (not shown here), indicating anomalous oceanic heat advection from the warm Bering Slope Current to the ice edge and/or from the deep basin onto the shelf.

Fig. 11 As in Fig. 9 but for the southern box in Fig. 1

The near compensation between dynamic and thermodynamic ice volume changes and the dominance of dynamic effects in the net ice volume change are prominent at the southern site. As shown in Fig. 10c, the anomalies of thermodynamic and dynamic tendencies

have a high correlation (−0.87) for year-round behavior and even higher correlation (−0.98) for winter months. The net ice volume tendency anomaly correlates fairly closely with the dynamic tendency anomaly, with a correlation of 0.66 (0.83 for winter).
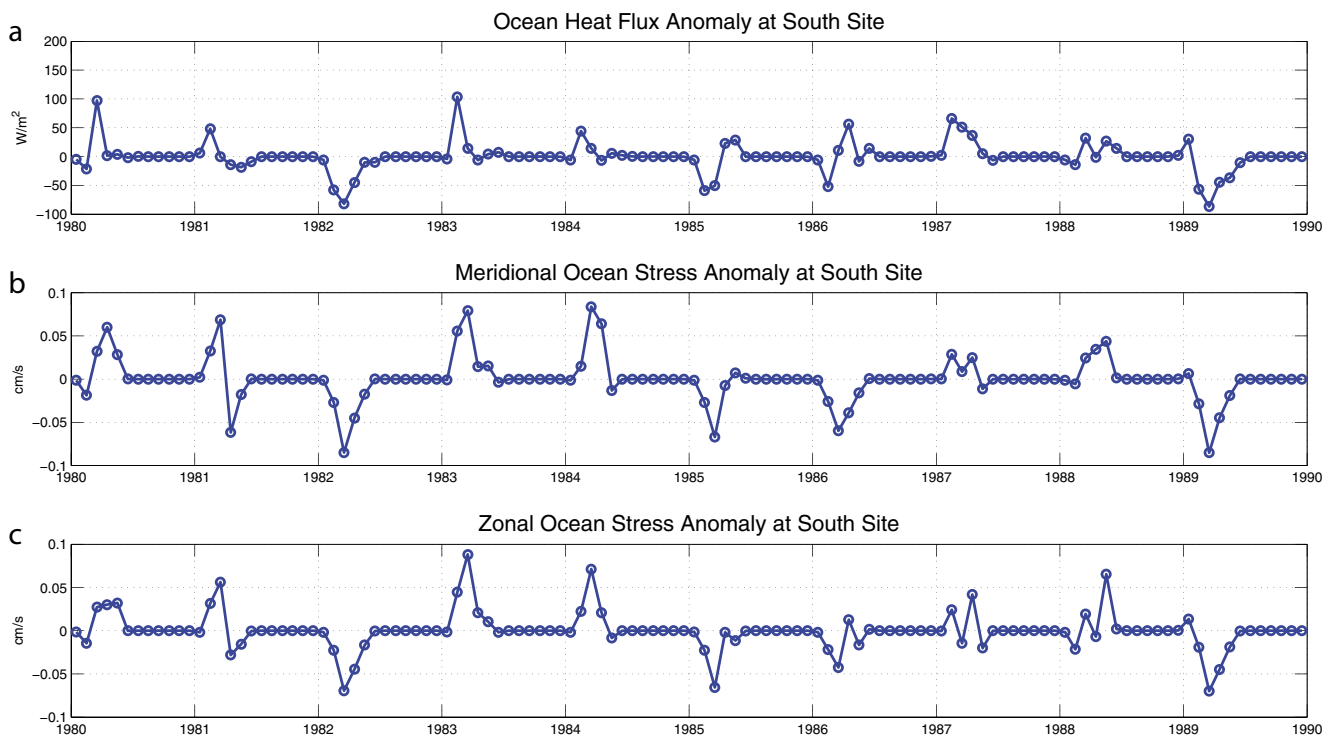

Fig. 12 **a** Ocean heat flux anomaly, **b** meridional ocean stress anomaly, and **c** zonal ocean stress anomaly averaged over the southern box in Fig. 1

In summary, for these characteristic local sites near ice margins with either land or ocean, the surface energy flux appears to play a dominant role in driving thermodynamic ice volume changes in the north, while oceanic heat flux appears to largely control ice melt around the ice edge in the south. Wind stress appears to largely drive ice motion, especially in the meridional direction. There is near compensation between dynamic and thermodynamic ice volume changes in both locations, especially in the south. Dynamic processes dominate the ice volume change anomalies at both of these local sites near two very different ice margins. But, the net ice volume changes are small in the north near the land boundary, and they are large in the south near the ocean boundary.

3.2.2 Local ice energy budget

The local budget of surface energy flux shows its dependence on location. At the northern growth site (Fig. 13), net surface energy flux (Fig. 13a) and its anomaly (Fig. 13b) are dominated by sensible heat flux from December to April when ice is abundant, indicating the important role of air temperature on surface energy flux. Both the shortwave and the longwave radiation are relatively constant from year to year, but shortwave radiation is only significant in spring and summer while longwave radiation is important in winter and spring. The net surface energy flux is negative during winter months, and it is nearly zero in late spring and summer. Both net surface energy flux and sensible heat flux are small in the 1982 and 1989

warm winters, and they are large in the 1983 and 1984 cold winters. These anomalies of surface energy flux could explain the weak ice growth in 1982 and 1989 and strong ice growth in 1983 and 1984 (Fig. 8), and they are consistent with warm air temperatures in 1982 and 1989 and cold air temperatures in 1983 and 1984 (Fig. 9).

In contrast, at the southern melt site (Fig. 14), winter net surface energy flux is small and negative, and it is mainly determined by the balance of negative longwave radiation, negative latent heat flux, and positive sensible heat flux in winter. The sensible heat flux is always positive along the ice edge where air temperature is warmer than ice surface temperature. The interannual variability of net surface energy flux still correlates with the sensible heat flux anomaly. Because sensible heat flux, latent heat flux, and longwave radiation are all dependent on ice surface temperature, significant correlations also exist between them.

In summary, in the north, net surface energy flux is dominated by sensible heat flux during winter months; along the ice edge, winter net surface energy flux is the combined effect of longwave radiation, latent heat flux, and sensible heat flux.

3.2.3 Local ice force balance

We also consider the force balances and ice motion at two local sites. The horizontal forces on the sea ice consist of wind stress on the ice, ocean stress on the ice, Coriolis force,
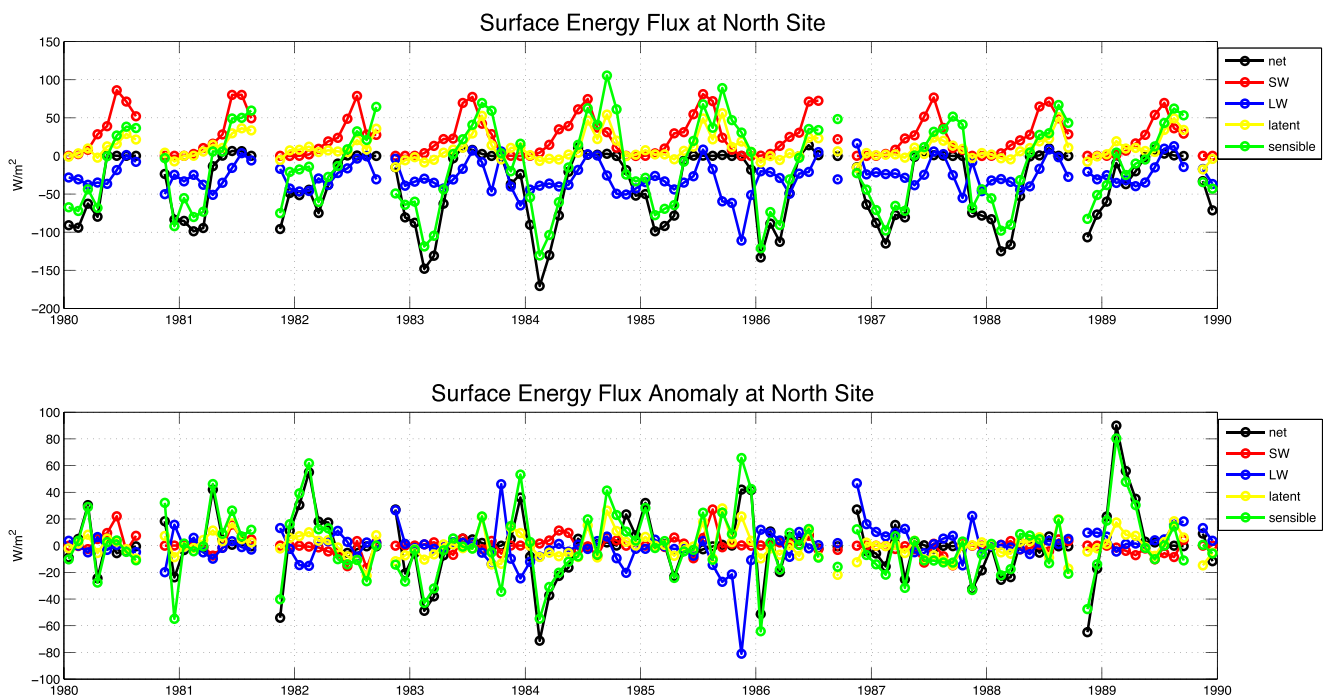

Fig. 13 **a** Net surface energy flux (*black*), net shortwave radiation (*red*), net longwave radiation (*blue*), latent heat flux (*yellow*), and sensible heat flux (*green*) averaged over the ice cover in the northern box in Fig. 1. If the area is ice-free, the values are not plotted. **b** Anomalies of net surface

energy flux (*black*), net shortwave radiation (*red*), net longwave radiation (*blue*), latent heat flux (*yellow*), and sensible heat flux (*green*) averaged over the ice cover in the northern box in Fig. 1. If the area is ice-free, the values are not plotted
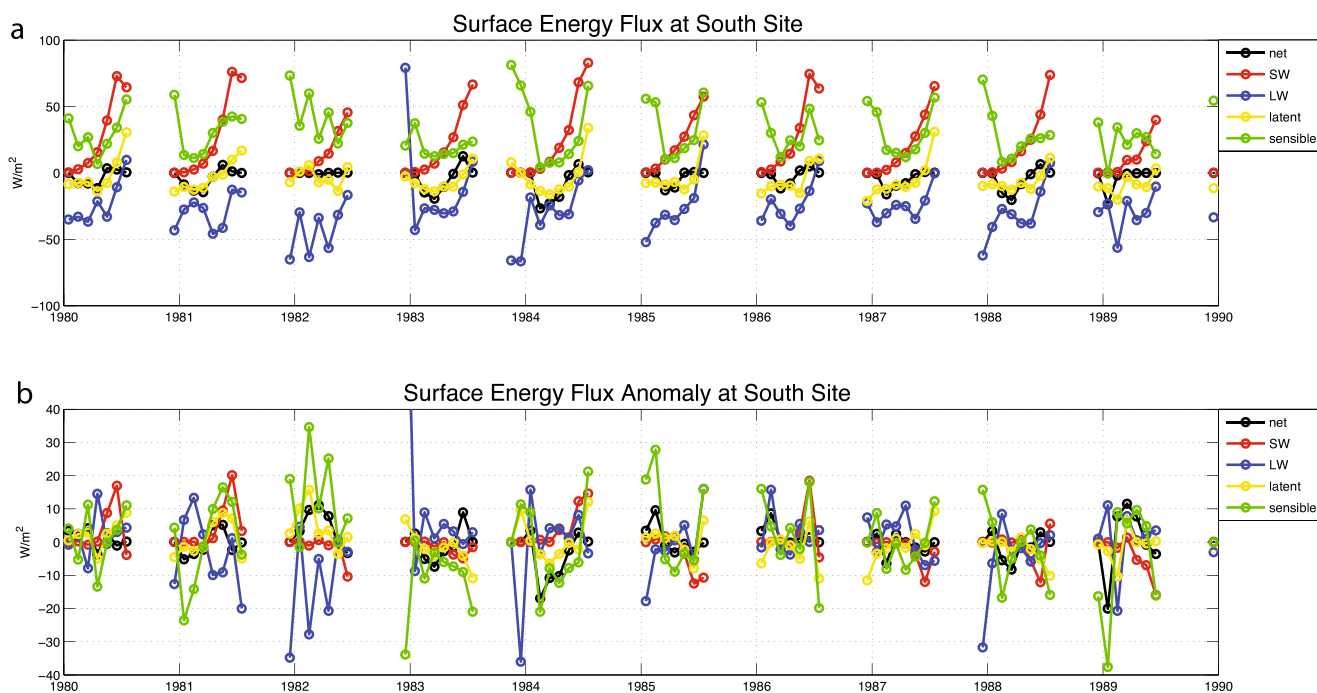
Fig. 14 As in Fig. 13, but for the southern box in Fig. 1

divergence of the internal ice stress tensor, and gravitational force due to sea surface slope.

For the northern site, as shown in Fig. 15a, b, the five forces are nearly in balance, producing nearly zero ice acceleration. The dominant forces are wind stress and ocean stress with opposite directions and similar magnitudes (Fig. 15a, b). In the meridional direction, wind stress is slightly stronger than the ocean stress (Fig. 15a). The meridional ice velocity (Fig. 15c) is consistent with the meridional wind stress (red curve in Fig. 15a). However, in the zonal direction, the ocean stress is slightly stronger than the wind stress (Fig. 15b), and the zonal ice velocity (Fig. 15d) is more consistent with the zonal ocean stress (blue curve in Fig. 15b). This indicates that at some northern locations near narrow straits such as this site, the zonal ice velocity is more related to ocean stress, while the meridional ice velocity is consistent with wind stress. The divergence of the internal ice stress is significant in this high ice concentration area (Fig. 15a, b), and it generally resists ice motion there (Fig. 15c, d). Note that the meridional stress due to sea surface slope is significant at this northern site (magenta curve in Fig. 15a), where there is a relatively large sea surface slope which forces the ice northward.

At the northern site, the sum of wind stress and ocean stress is the same order as other force terms, as shown in Fig. 15e, f. In the meridional direction (Fig. 15e), the northward divergence of the internal ice stress tensor and the force due to sea surface slope are opposed by the southward residual of wind stress and ocean stress, as well as the Coriolis force. Note that the northward stress due to sea surface slope is as strong as the meridional divergence of the internal ice stress. The

meridional Coriolis force is also large due to rapid zonal ice motion through the strait. In the zonal direction (Fig. 15f), the force balance is mainly between divergence of the internal ice stress and the residual sum of wind stress and ocean stress.

For the southern site, the forces are also in approximate balance (Fig. 16a, b). The ice velocity (Fig. 16c, d) is consistent with the wind stress (red curves in Fig. 16a, b), which is almost balanced by the opposite ocean stress (blue curves in Fig. 16a, b). The divergence of the internal ice stress is weak and southward in winter (Fig. 16a, b). There is nearly no force due to sea surface slope (Fig. 16a, b), implying a relatively flat sea surface. In the meridional direction (Fig. 16a, e), wind stress is nearly balanced by ocean stress. The northward Coriolis force balances southward divergence of the internal ice stress. In the zonal direction (Fig. 16f), the residual sum of wind stress and ocean stress largely balances the Coriolis force.

In summary, wind stress on the ice, ocean stress on the ice, the Coriolis force, divergence of the internal ice stress, and gravitational force due to sea surface slope nearly balance to produce a very small net force on the ice. The ice motion is largely driven by the wind stress, especially in the meridional direction. At some northern locations near narrow straits, however, the ice motion follows the direction of the ocean stress. The divergence of the internal ice stress can be important at some local locations near the land boundaries in the north (where it is largely balanced by the wind stress and ocean stress). There, the divergence of the internal ice stress resists the ice motion. It is small, however, in the central and southern ice-covered area. The Coriolis force and gravitational force due to sea surface
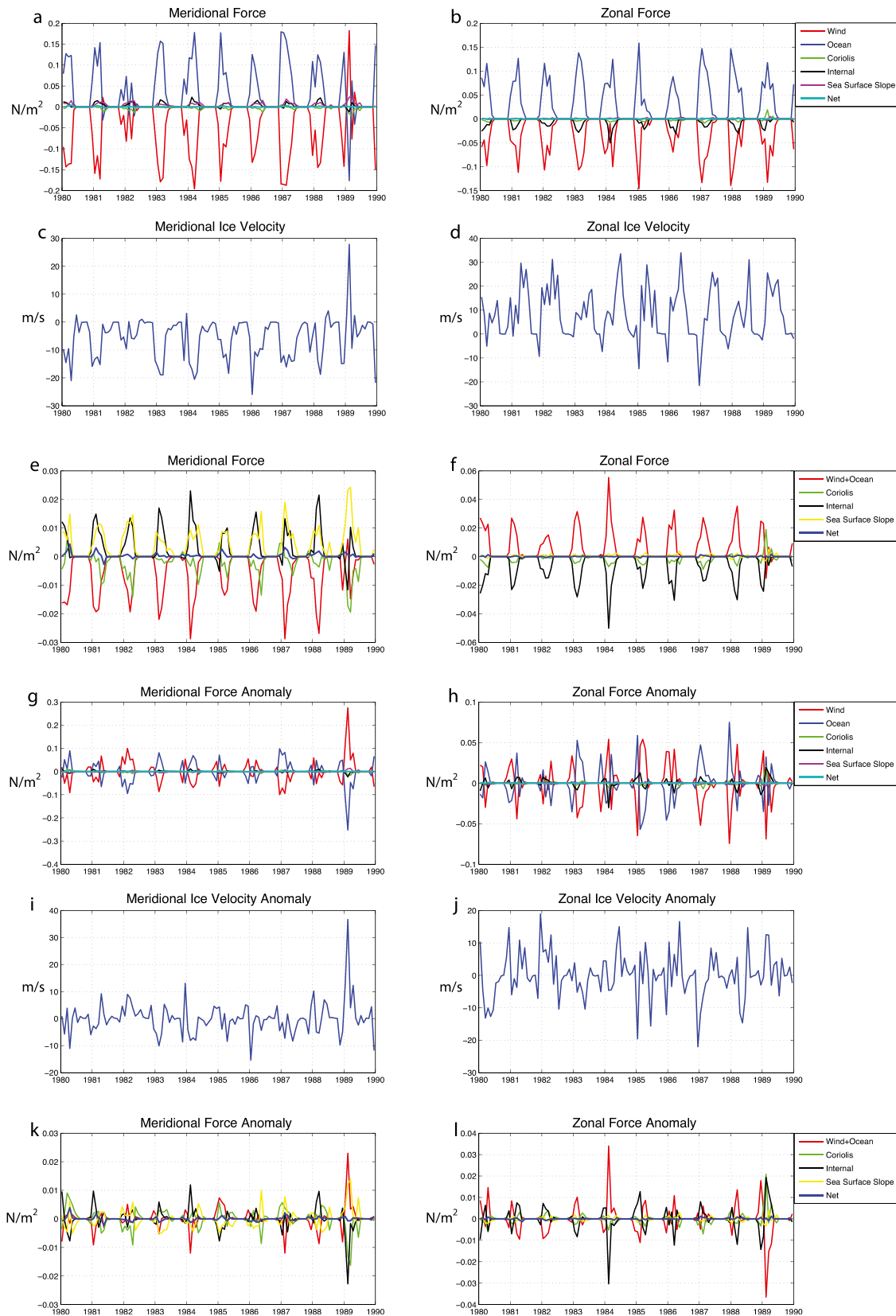
North Site

Fig. 15 As in Fig. 7, but averaged over the northern box indicated in Fig. 1
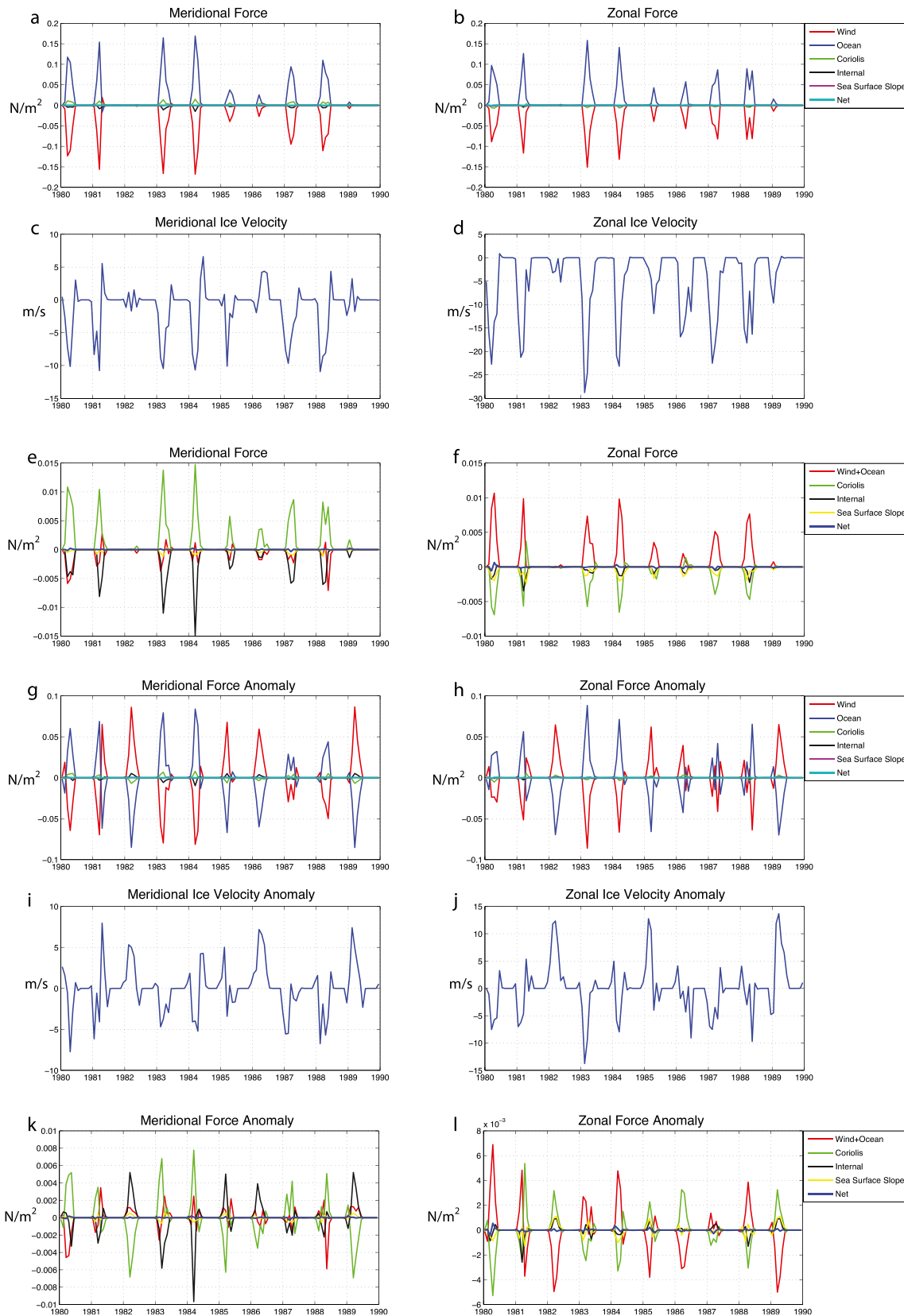
South Site

Fig. 16 As in Fig. 7, but averaged over the southern box indicated in Fig. 1

slope are typically small, but the Coriolis force becomes relatively important near the ice edge in the south, and the meridional force due to sea surface slope can be significant in the north near land.

3.3 Anomalous events

We next examine the two largest Bering Sea ice anomaly events during the 1980–1989 time interval, which occur with opposite anomalous ice and atmosphere/ocean conditions.

3.3.1 February 1989

In February 1989, the ice volume tendency anomaly reached its most negative value over the 1980–1989 period (Fig. 4b). Figure 17 shows the spatial structures of several ice variables to help determine the regional processes affecting this anomalous state. The net ice volume tendency anomaly is negative over the extensive ice-covered area in the southern and central regions, and it is positive along the regions to the south of the land boundaries, as shown in Fig. 17d. This pattern appears to be driven by the combined forcing of anomalous warm air and anomalous southerly wind, as shown in Fig. 18a.

The southerly wind (Fig. 18a) drives ice transport northward (Fig. 17c). This causes a negative dynamic tendency anomaly in the south and middle of the ice-covered area and a positive dynamic tendency anomaly near the northern coasts and islands (Fig. 17f). The ice transport anomaly through the Bering Strait is toward the Arctic Ocean (Fig. 17c), which causes the total dynamic tendency anomaly in the Bering Sea to be negative (Fig. 17f).

The wind stress anomaly on the ice (Fig. 18b) and the ocean stress anomaly on the ice (Fig. 18d) have opposing signs with similar magnitude. As shown in Figs. 17c and 9d, the spatial distribution of the magnitude of the ice velocity anomaly is consistent with structures seen in the magnitude of the wind stress anomaly. The direction of the ice velocity anomaly is rotated to the right of the wind stress anomaly with an angle of approximately 30°. This implies that the wind stress anomaly drives the ice motion anomaly, and the ocean stress anomaly resists the ice motion anomaly and nearly balances the wind stress anomaly.

The thermodynamic tendency anomaly consists of an ice volume decrease in the north and an ice volume increase along the southern ice edge, as shown in Fig. 17e. This can be understood by partitioning the thermodynamic tendency anomaly into ice growth anomalies (including congelation ice growth, frazil ice growth, and snow ice formation; not shown here) and ice melt anomalies (including basal ice melt, lateral ice melt, and top ice melt; not shown here). We find that the northern negative anomaly of the thermodynamic tendency is largely due to congelation ice growth, whereas the southern positive anomaly is dominated by reduced basal ice
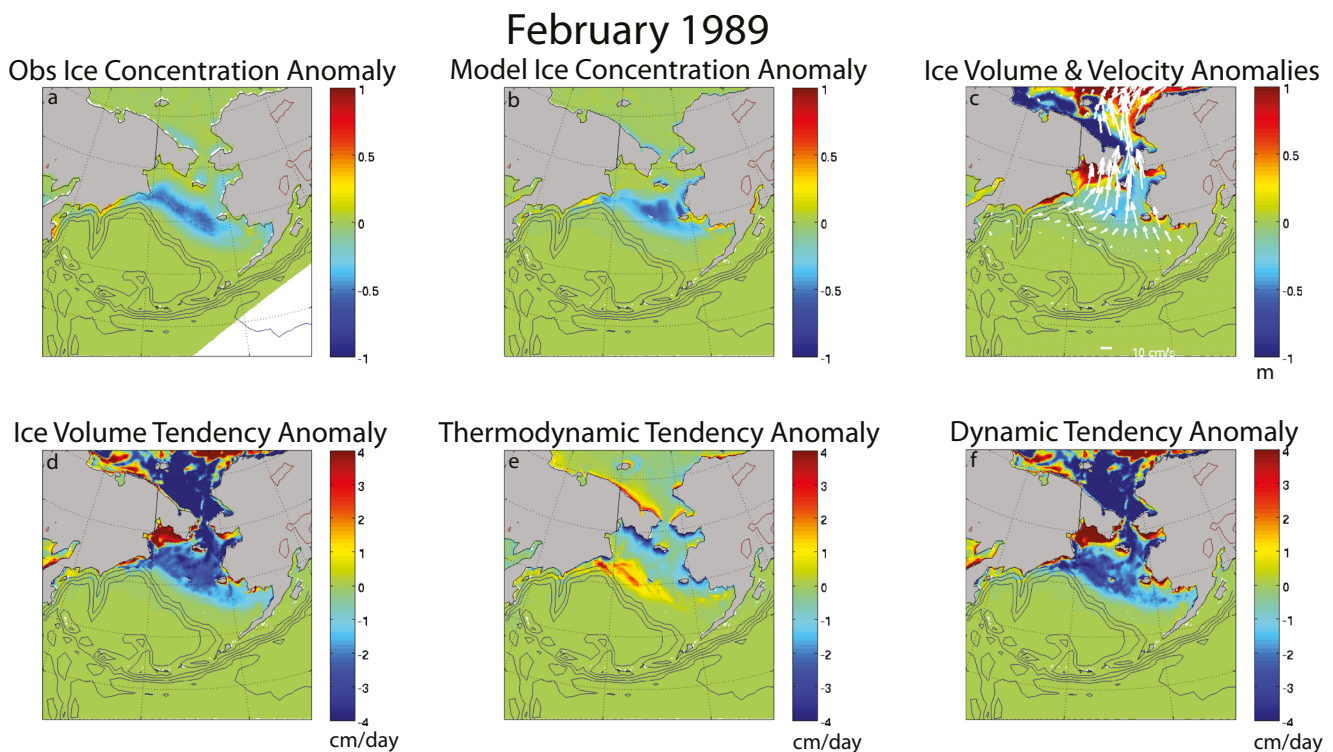

Fig. 17 **a** February 1989 observed ice concentration anomaly, **b** modeled ice concentration anomaly, **c** ice volume anomaly (*colors*) and ice velocity anomaly (*arrows*), **d** net ice volume tendency anomaly, **e** thermodynamic ice volume tendency anomaly, and **f** dynamic ice volume tendency anomaly
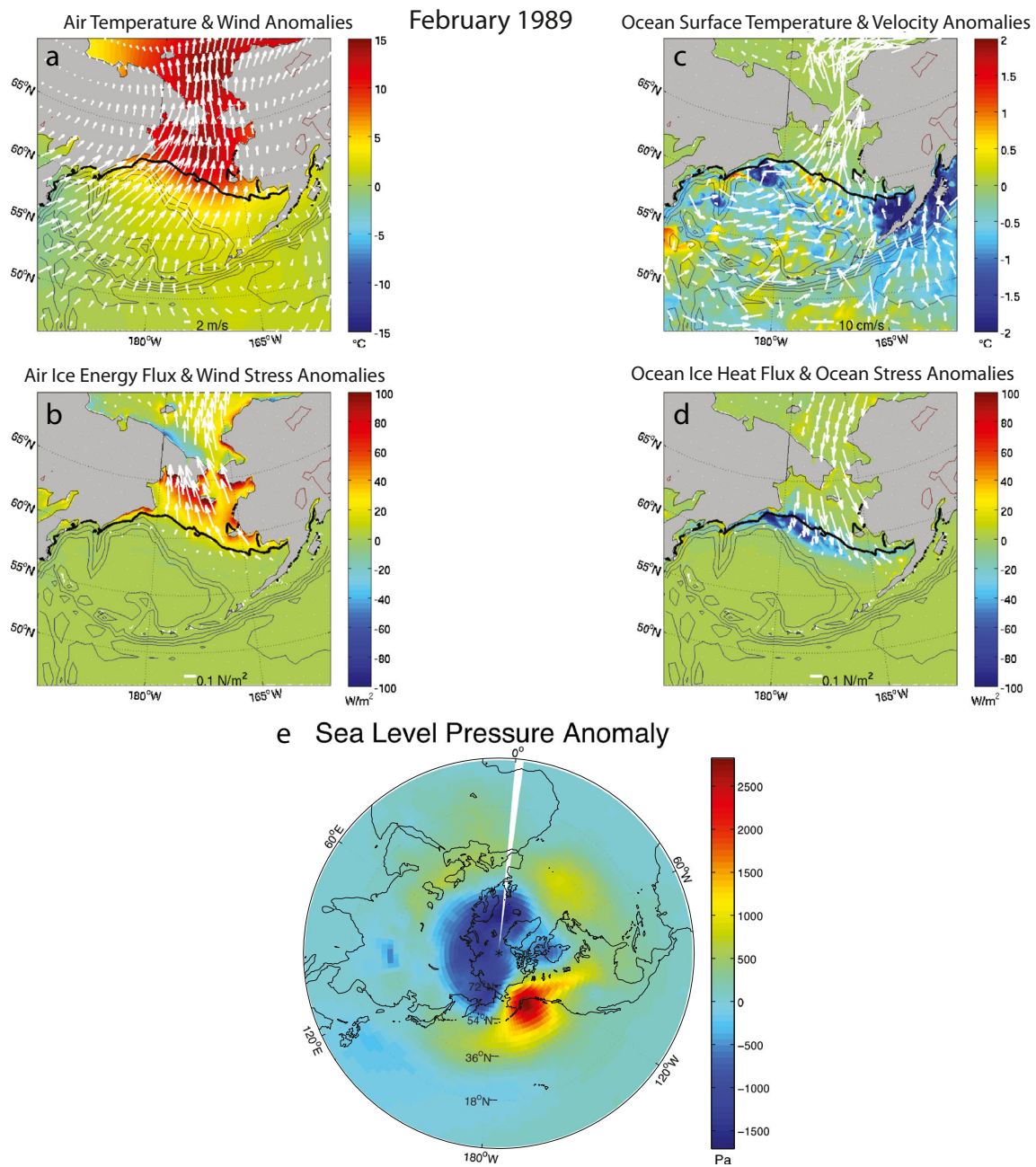
Fig. 18 **a** February 1989 surface air temperature and wind anomalies, **b** atmosphere-ice energy flux and wind stress anomalies, **c** ocean surface temperature and velocity anomalies, **d** ocean-ice heat flux and ocean stress anomalies in the Bering Sea, and **e** sea level pressure anomaly in the northern hemisphere. Heat fluxes into the ice are indicated by positive values. The *thick black line* in **a**–**d** represents the 15 % ice concentration contour

melt. This dipole pattern of the thermodynamic tendency anomaly corresponds to the air-ice energy flux anomaly acting in the north (Fig. 18b) and the ocean-ice heat flux anomaly acting in the south (Fig. 18d). The 15 % ice concentration contour approximately marks the boundary between these two regions. We can see that the atmospheric thermal forcing acts weakly over the extensive ice-covered region but strongly around the northern coastal polynyas, and oceanic thermal forcing primarily acts in a narrow band along the ice edge.

Warm surface air temperature (Fig. 18a) can reduce surface heat flux from ice to atmosphere (Fig. 18b) and thus suppress ice growth (Fig. 17e). This occurs on the large scale almost everywhere over the ice-covered area in the Bering Sea. Also, dynamical ice thickening due to ice motion against the northern coasts of the Bering Sea (Fig. 17f) further weakens ice growth (Fig. 17e) there. On the other hand, the anomalous northward ice motion causes reduced ice concentration near the southern ice edge, causing reduced bottom ice melting
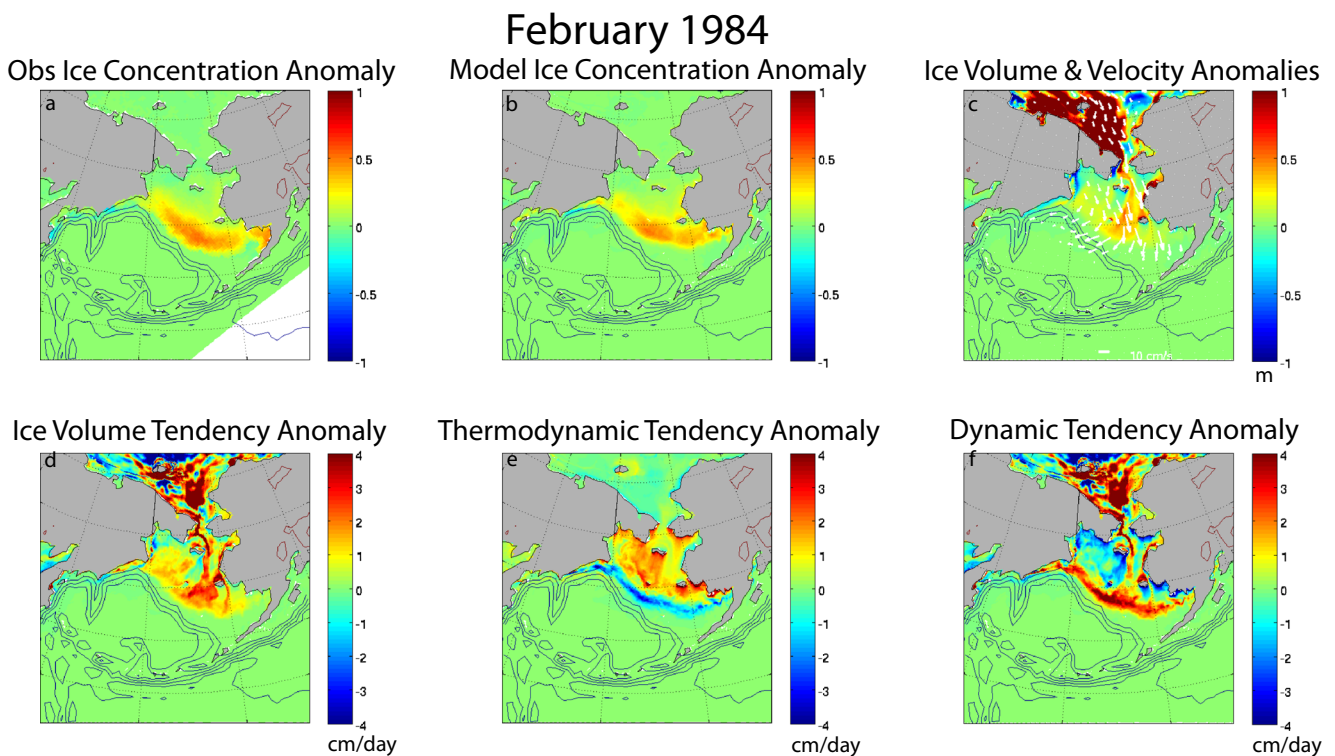
February 1984

Fig. 19 As in Fig. 17, but for February 1984

from the ocean (Fig. 17e) despite the warm Bering Slope Current (Fig. 17c) because less ice is left to melt.

3.3.2 February 1984

In February 1984, the ice volume tendency anomaly is the most positive during the 1980–1989 period (Fig. 4b). The net ice volume tendency anomaly is positive almost everywhere in the ice-covered area, as shown in Fig. 19d. Anomalous thermodynamic ice growth occurs in the middle and north of the ice interior, and anomalous thermodynamic ice melt occurs along a narrow band along the ice edge (Fig. 19e). Dynamically, ice is anomalously transported away from the northern coastal region and into the southern ice edge region (Fig. 19c, f). Comparing the net ice volume tendency and thermodynamic/dynamic tendencies (Fig. 19d–f), we see that in the ice interior, thermodynamic effects are slightly stronger than dynamic effects, and around the coastal polynyas, thermodynamic effects nearly balance dynamic effects, and dynamic effects dominate along the ice edge.

The anomalous southward ice motion (Fig. 19c) appears to be driven by a northerly wind anomaly (Fig. 20a). The anomalously cold surface air temperature (Fig. 20a) promotes larger heat loss from ice to atmosphere (Fig. 20b) and thus larger ice growth rates in the north, especially around the coastal polynyas (Fig. 19e). Ice advection into the southern warm ocean (Fig. 19c, f) produces larger basal melt rates along the ice edge

(Fig. 19e). The cooling of sea surface temperatures around the ice edge (Fig. 20c) may be a consequence of the anomalous ice transport into the region (Fig. 19e).

3.3.3 Atmosphere circulation patterns in February 1989 and February 1984

The position of the Aleutian Low largely determines ice variations in the Bering Sea (Rogers 1981; Cavalieri and Parkinson 1987; Niebauer 1998; Rodionov et al. 2005, 2007). The winter sea ice extent is also associated with storm tracks (Overland and Pease 1982; Rodionov et al. 2007) and the local atmospheric variability related to winds (Sasaki and Minobe 2005).

On the large scale, a very high sea level pressure anomaly (~20 hPa higher than normal) occurs in Feb. 1989, centered near the Gulf of Alaska, as shown in Fig. 18e. There is also anomalous low pressure over the Arctic, especially on the Siberian side in Feb. 1989 (Fig. 18e). These sea level pressure anomalies induce anomalous southerly winds over the Bering Sea (Fig. 18a). The high pressure anomaly can be seen over Alaska in Jan 1989, and it moves to the west and becomes weaker in March 1989. In contrast, anomalous low pressure in the east and anomalous high pressure in the northwest (Fig. 20e), favoring anomalous northerly winds (Fig. 20a), occur in Feb. 1984 when the ice volume tendency is highest (Fig. 19d).

These two anomalous events are associated with substantially different patterns of the Aleutian Low. In Feb. 1989, the
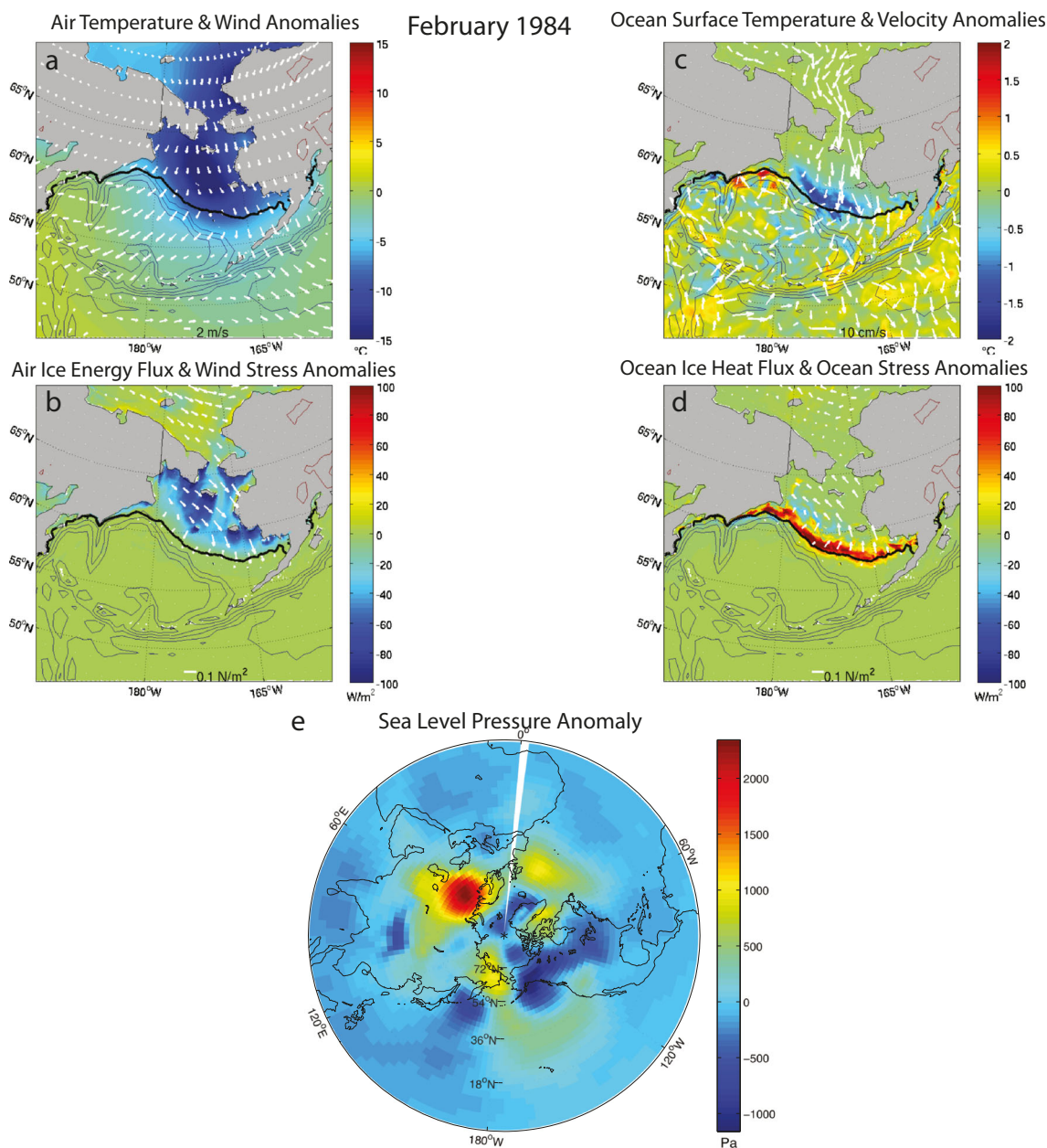
Fig. 20 As in Fig. 18, but for February 1984

Aleutian Low was centered at the southwestern corner of the Bering Sea, while in Feb. 1984, the Aleutian Low had two split centers, one around the Gulf of Alaska and the other further southwest of the Aleutian Islands. The total distribution of sea level pressure produces anomalous southerly wind in Feb. 1989 (Fig. 18a) and anomalous northerly wind in Feb. 1984 (Fig. 20a).

These results resemble the results of Rodionov et al. (2005, 2007). The warm event in Feb. 1989 is classified as a W1 type of atmospheric circulation, and the cold event in Feb. 1984 is classified as a C1 type in Table 1 of the Rodionov et al. (2005). Type W1 is defined as an Aleutian Low with one single center

located north of 51° N and between 156° W and 173° W. Type C1 is defined as a split Aleutian Low with the western center south of 52° N and the eastern center not further east than 140° W. These types correspond to warm and cold surface air temperatures for winter months in the Bering Sea. Type W1 is related to transient storms, when most storms enter the Bering Sea along the secondary storm track off the Siberian coast, and fewer storms enter along the primary storm track in the central and eastern North Pacific. Type C1 is accompanied by eastward extension of a stronger Siberian High. C1 has storms penetrating not so far north as W1 along the Siberian coast, and it has northerly flow on the east periphery of the

upper atmospheric ridge. Additionally, they show that the main climate indices for the North Pacific (NP, PDO, and PNA) poorly represent the winter air temperatures in the Bering Sea. Instead, the warm event in Feb. 1989 is associated with an enhanced storm track off the Siberian coast. This implies local forcing of the anomalous event from the intrinsic variability associated with storm tracks, rather than from large-scale climate variations.

3.4 Sea ice transport variations through the Bering Strait

The ice transport through the Bering Strait provides a form of freshwater and energy flux between the Bering Sea and the Arctic Ocean and influences the amount of freshwater and heat in the upper layer of the western Arctic Ocean.

Monthly mean ice mass transports on the northern and eastern sides of each grid cell are archived from the model. The ice volume transport through the Bering Strait is calculated in Fig. 21 (monthly, 1980–1989). The ice transport through the Bering Strait shows large interannual variability. Notably, in Feb. 1989, the northward ice transport is extremely high when strong southerly winds dominate the region. In contrast, in Feb. 1984, the southward ice transport is the largest during this time period, when the northerly wind is very strong. This suggests that winds cause the extreme anomalies of ice transport.

As expected, the ice volume transport through the Bering Strait (Fig. 21) agrees well with the dynamic ice volume tendency integrated over the whole Bering Sea (blue curve

in Fig. 4a). The dynamic ice volume tendency in the Bering Sea is determined by the ice transport at the boundaries of the Bering Sea. The Bering Strait is the most important boundary for ice transport. At other boundaries with the open ocean, there is almost no ice transport. Note that there is a very small amount of ice transport along the coast of the Kamchatka Peninsula, but the amount is insignificant relative to the ice transport through the Bering Strait. Therefore, the ice transport through Bering Strait essentially indicates the integrated Bering Sea ice volume change due to dynamics.

4 Discussion

In the Bering Sea, the ice volume tendency is dominated by thermodynamic processes on the large scale, while dynamic effects are important locally, especially near the ice margins with ocean and land. Local thermodynamic and dynamic ice volume tendencies usually have opposite signs with similar magnitudes, producing stable ice volume. However, the anomalies of thermodynamic and dynamic tendencies can have the same sign to produce extreme anomalous events. Near the ice margins, the net ice volume change is usually dominated by dynamics. The near compensation between thermodynamic and dynamic tendencies, and the dominance of dynamic tendencies, occurs most prominently near the southern ice edge where ice variations are large, and it occurs less near the northern coastal polynyas where ice variations are small. In the ice interior, the dynamic effect is
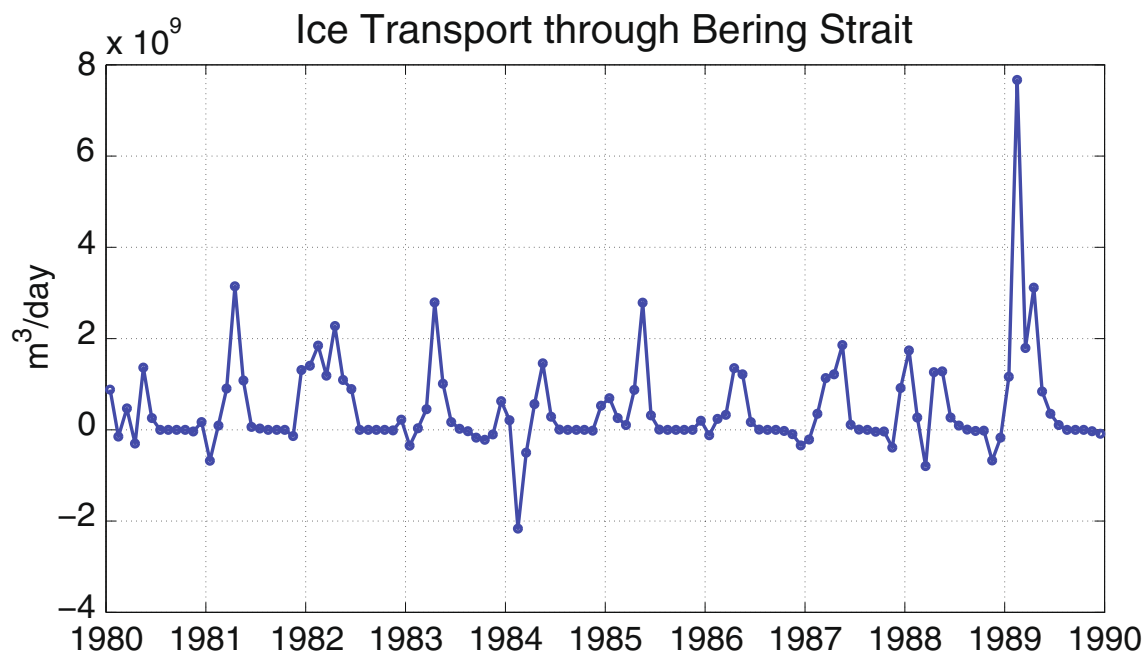

Fig. 21 Modeled sea ice transport through the Bering Strait for 1980–1989

small, and the thermodynamic effect determines the net ice volume change.

The thermodynamic ice volume tendency correlates well with surface energy fluxes and surface air temperatures in winter on the large scale. Locally in the central and northern parts of the Bering Sea, atmosphere-ice energy fluxes control ice growth, while ocean-ice heat flux controls basal ice melting around the southern ice edge. Surface energy flux between the ice and the atmosphere is dominated by sensible heat flux, and the contribution from net longwave radiation is also large.

Monthly mean ice motion is nearly in phase with wind stress, especially in the meridional direction. Ocean stress can be important in driving ice motion near the narrow straits in the north. Wind stress and ocean stress have similar and large magnitudes with opposing signs. Divergence of the internal ice stress is large near the land boundaries in the north, and it is small in the central and southern parts of the ice-covered area. The Coriolis force and the gravitational force due to sea surface slope are generally small.

The local and regional atmospheric and oceanic forcing of the Bering Sea ice was also examined to determine the details of the local balances controlling the ice. Our results are generally consistent with other studies. Some studies show that the climatic forcing of the Bering Sea ice variability arises from local processes (Fang and Wallace 1994, Sasaki and Minobe 2005), rather than being associated with any prominent large-scale remote climate indices. Wind anomalies over the Bering Sea are important for the interannual variability of sea ice. Many studies indicate the correspondence of anomalous northerly wind and increased sea ice in the Bering Sea (Niebauer 1980, Walsh and Sater 1981, Fang and Wallace 1994, Sasaki and Minobe 2005). At the same time, surface air temperature anomalies are related to advection by winds on the large scale (e.g., Deser et al. 2000).

In terms of spatial distributions, thermodynamic processes affect large-scale ice volume changes rather uniformly over the ice-covered area, and thus, the integrated effect is large. In contrast, dynamic effects produce small-scale features, and they are more important near the ice margins with ocean and land than in the ice interior. Therefore, both in time and in space, thermodynamic effects contribute to low-frequency ice variations, and dynamic effects contribute to higher frequency variations of sea ice in the Bering Sea.

The interactions between sea ice thickness and thermodynamic and dynamic processes are also considered. Both thermodynamic and dynamic processes cause ice thickness to change and ultimately determine the ice thickness. On the other hand, ice thickness influences the thermodynamic and dynamic ice volume tendencies in different ways. Thin ice grows faster thermodynamically, and thick ice contributes to larger dynamic ice volume changes in the presence of a convergent ice velocity field. We find that thermodynamic effects dominate the large-scale sea ice variability in the Bering Sea.

Our results are consistent with Walsh et al. (1985)'s result that thermodynamic processes contribute more to ice anomalies near the ice edge. Their Fig. 15 shows that thermodynamic processes dominate the seasonal cycle of ice mass change in the Bering Sea, small dynamic effects oppose the thermodynamic effect on an annual mean basis, and ice is transported from the eastern to the western Bering Sea. Their Fig. 17 shows that even on interannual timescales, thermodynamic processes correlate with the ice mass change both in the western and in the eastern Bering Sea. This is in contrast to the Arctic Ocean, where they find that dynamic effects dominate in winter, spring, and fall, whereas thermodynamic effects dominate in summer.

A model forced with reanalysis fluxes has limitations since ocean and sea-ice feedbacks with the atmosphere are not part of the simulation. Feedback effects when coupling the sea ice and ocean to an active atmosphere at this resolution is the subject of current research and a vital step toward understanding long-term changes and fluctuations of the ice-ocean system. An appropriate first step, however, is to understand and document ocean and sea ice behavior before coupling to an active atmosphere where biases can result from each of the component models and their interactions.

5 Conclusions

Using a high-resolution ice-ocean model, the basin-scale and local balances of sea ice in the Bering Sea have been examined. The model produces variations in total ice area anomalies that are highly correlated with observations. The variations in the model ice volume are largely controlled by thermodynamic forcing via the surface energy flux, which in turn is dominated by sensible heat flux. The sensible heat flux in this simulation is computed using a bulk formula that includes model surface temperatures and CORE2 surface air temperatures. This suggests that the specified surface air temperature, which correlates with the observed sea ice distribution, may control the ice volume tendency in this simulation, because sensible heat flux becomes large when the model surface temperature diverges from the specified surface air temperature. This also may explain the similarly high levels of skill for ice area simulations that were obtained by Danielson et al. (2011).

Thermodynamic processes dominate the ice volume changes in the Bering Sea on the large scale. In contrast, dynamic processes are important on the local scale near ice margins (both oceanic and land), where local dynamic and thermodynamic ice volume changes have opposite signs with similar amplitudes. The thermodynamic ice volume change is dominated by surface energy flux between the ice and the atmosphere, except near the southern ice edge where it is largely controlled by ocean-ice heat flux. Ice motion is generally consistent with winds driving the

flow, but ice motion largely follows ocean currents near certain straits in the north.

Two key climate events, strong ice growth with cold air temperature and northerly wind anomalies in February 1984 and weak ice growth with warm air temperature and southerly wind anomalies in February 1989, are studied in detail. The processes controlling the ice changes in other years are generally similar to these two events. These events reveal spatial patterns of ice growth anomalies in the north accompanied by ice melt anomalies along the ice edge in the south, with dynamic anomalies transporting ice from the north to the south. These climate events are associated with the position of the Aleutian Low, which appears to be regulated by local processes rather than large-scale climate events (Rodionov et al. 2005, 2007).

This study of interannual ice variations in the Bering Sea during 1980–1989 can form a baseline for a longer-term ice variability study, including changes in the 1990s and 2000s, as well as possibly the impacts of global warming. Mesoscale eddy effects could also be studied through the comparison of high-resolution and low-resolution versions of the model, using higher-frequency temporal archiving of the model output. Tests of the viability of the tidal mixing parameterization, currently used in CESM at standard climate horizontal resolution (~1°), will be attempted in high-resolution CESM shortly. A fully coupled atmosphere/sea-ice/ocean simulation can be examined and compared with the current uncoupled model run in order to better understand the interaction between sea ice, the atmosphere, and the ocean in the presence of internal variability of the climate system.

References

Auad G, Miller AJ (2008) The role of tidal forcing in the Gulf of Alaska's circulation. Geophys Res Lett 35:L04603

Bitz CM, Lipscomb WH (1999) An energy-conserving thermodynamic model of sea ice. J Geophys Res 104(C7):15669–15677

Bitz CM, Holland MM, Hunke EC, Moritz RE (2005) Maintenance of the sea-ice edge. J Clim 18(15):2903–2921

Cavalieri DJ, Parkinson CL (1987) On the relationship between atmospheric circulation and the fluctuations in the sea ice extents of the Bering and Okhotsk seas. J Geophys Res 92(C7):7141–7162

Cheng W, Curchitser E, Ladd C, Stabeno P, Wang M (2014) Influences of sea ice on the Eastern Bering Sea: NCAR CESM simulations and comparison with observations. Deep-Sea Res. Part II Top. Stud. Oceanogr. doi:10.1016/j.dsr2.2014.03.002

Comiso JC (2000) Bootstrap sea ice concentrations from Nimbus-7SMMR and DMSP SSM/I-SSMIS. Version 2. Boulder, Colorado USA: NASA DAAC at the National Snow and Ice Data Center

Connolley WM, Gregory JM, Hunke E, McLaren AJ (2004) On the consistent scaling of terms in the sea-ice dynamics equation. J Phys Oceanogr 34(7):1776–1780

Craig AP, Vertenstein M, Jacob R (2012) A new flexible coupler for earth system modeling developed for CCSM4 and CESM1. Int J High Perform C 26:31–42

Danielson S, Curchitser E, Hedstrom K, Weingartner T, Stabeno P (2011) On ocean and sea ice modes of variability in the Bering Sea. J Geophys Res 116:C12034

Deser C, Walsh JE, Timlin MS (2000) Arctic sea ice variability in the context of recent atmospheric circulation trends. J Clim 13(3):617–633

Dukowicz JK, Smith RD (1994) Implicit free-surface method for the Bryan-Cox-Semtner ocean model. J Geophys Res 99: 7991–8014

Fang Z, Wallace JM (1994) Arctic sea ice variability on a timescale of weeks and its relation to atmospheric forcing. J Clim 7(12):1897–1914

Fetterer F, Knowles K, Meier W, Savoie M (2002, updated daily). Sea Ice Index. Boulder, Colorado USA: National Snow and Ice Data Center. Digital media

Griffies SM, Biastoch A, Boning C, Bryan F, Danabasoglu G, Chassignet EP, England MH, Gerdes R, Haak H, Hallberg RW, Hazeleger W, Jungclaus J, Large WG, Madec G, Pirani A, Samuels BL, Scheinert M, Gupta AS, Severijns CA, Simmons HL, Treguier AM, Winton M, Yeager S, Yin J (2009) Coordinated Ocean-ice Reference Experiments (COREs). Ocean Model 26:1–46

Griffies SM, Winton M, Samuels B, Danabasoglu G, Yeager S, Marsland S, Drange H, Bentsen M (2012) Datasets and protocol for the CLIVAR WGOMD Coordinated Ocean sea-ice Reference Experiments (COREs). WCRP, Report No. 21/2012

Haidvogel DB, Arango H, Budgell WP, Cornuelle BD, Curchitser E, Di Lorenzo E, Fennel K, Geyer WR, Hermann AJ, Lanerolle L et al (2008) Ocean forecasting in terrain-following coordinates: formulation and skill assessment of the regional ocean modeling system. J Comput Phys 227(7):3595–3624

Hermann AJ, Stabeno PJ, Haidvogel DB, Musgrave DL (2002) A regional tidal/subtidal circulation model of the southeastern Bering Sea: development, sensitivity analyses and hindcasting. Deep-Sea Res Part II Top Stud Oceanogr 49:5495–5967

Holland MM, Serreze MC, Stroeve J (2010) The sea ice mass budget of the arctic and its future change as simulated by coupled climate models. Clim Dynam 34(23):185–200

Hunke EC, Dukowicz JK (1997) An elastic-viscous-plastic model for sea ice dynamics. J Phys Oceanogr 27(9):1849–1867

Kimura N, Wakatsuchi M (2000) Relationship between sea-ice motion and geostrophic wind in the northern hemisphere. Geophys Res Lett 27(22):3735–3738

Kimura N, Wakatsuchi M (2001) Mechanisms for the variation of sea ice extent in the northern hemisphere. J Geophys Res 106(C12):31319–31331

Large WG, Yeager SG (2004) Diurnal to decadal global forcing for ocean and sea-ice models: the data sets and flux climatologies. National Center for Atmospheric Research

Large WG, Yeager SG (2009) The global climatology of an interannually varying air–sea flux data set. Clim Dynam 33(2-3):341–364

Li L, McClean JL, Miller AJ, Eisenman I, Hendershott MC, Papadopoulis CA (2014) Processes driving sea ice variability in the Bering Sea in an eddying ocean/sea ice model: mean seasonal cycle. Ocean Model., in press

Linkin ME, Nigam S (2008) The north pacific oscillation-west pacific teleconnection pattern: mature-phase structure and winter impacts. J Clim 21(9):1979–1997

Lipscomb WH, Hunke EC (2004) Modeling sea ice transport using incremental remapping. Mon Weather Rev 132:1341–1354

Liu Z, Liu Y, Wu L, Jacob R (2007) Seasonal and long-term atmospheric responses to reemerging North Pacific Ocean variability: a combined dynamical and statistical assessment. J Clim 20(6):955–980

Matthewman NJ, Magnusdottir G (2011) Observed interaction between pacific sea ice and the western pacific pattern on intraseasonal time scales. J Clim 24(19):5031–5042

McClean JL, Bader DC, Bryan FO, Maltrud ME, Dennis JM, Mirin AA, Jones PW, Kim YY, Ivanova DP, Vertenstein M, Boyle JS, Jacob RL, Norton N, Craig A, Worley PH (2011) A prototype two-decade fully-coupled fine-resolution CCSM simulation. Ocean Model 39: 10–30

McClean JL, Hunke EC, Bailey D, Papadopoulos C, Yulaeva E (2014) Multi-decadal CORE-forced global 0.1-deg coupled ocean/sea-ice simulations using the Community Earth System Model, in preparation

Muench RD, Ahlnas K (1976) Ice movement and distribution in the Bering Sea from March to June 1974. J Geophys Res 81(24): 4467–4476

Niebauer HJ (1980) Sea ice and temperature variability in the eastern Bering Sea and the relation to atmospheric fluctuations. J Geophys Res 85(C12):7507–7515

Niebauer HJ (1983) Multiyear sea ice variability in the eastern Bering Sea: an update. J Geophys Res 88(C5):2733–2742

Niebauer HJ (1988) Effects of el nino-southern oscillation and north pacific weather patterns on interannual variability in the subarctic Bering Sea. J Geophys Res 93(C5):5051–5068

Niebauer HJ (1998) Variability in Bering Sea ice cover as affected by a regime shift in the north pacific in the period 1947–1996. J Geophys Res 103(C12):27717–27737

Niebauer HJ, Day RH (1989) Causes of interannual variability in the sea ice cover of the eastern Bering Sea. GeoJournal 18(1):45–59

Overland JE, Pease CH (1982) Cyclone climatology of the Bering Sea and its relation to sea ice extent. Mon Weather Rev 110(1):5–13

Overland JE, Adams JM, Bond NA (1999) Decadal variability of the Aleutian Low and its relation to high-latitude circulation. J Clim 12(5):1542–1548

Pease CH (1980) Eastern Bering Sea ice processes. Mon Weather Rev 108(12):2015–2023

Pease CH, Overland JE (1984) An atmospherically driven sea-ice drift model for the Bering Sea. Ann Glaciol 5:111–114

Reynolds M, Pease CH, Overland JE (1985) Ice drift and regional meteorology in the southern Bering Sea: results from MIZEX West. J Geophys Res 90(C6):11967–11981

Rigor I, Colony R, Martin S (2000) Variations in surface air temperature observations in the Arctic, 1979–1997. J Clim 13:896–914

Rodionov SN, Overland JE, Bond NA (2005) The Aleutian Low and winter climatic conditions in the Bering Sea. Part I: classification. J Climate 18(1):160–177

Rodionov SN, Bond NA, Overland JE (2007) The Aleutian Low, storm tracks, and winter climate variability in the Bering Sea. Deep-Sea Res Part II Top Stud Oceanogr 54(23):2560–2577

Rogers JC (1981) The North Pacific oscillation. J Climatol 1(1):39–57

Sasaki YN, Minobe S (2005) Seasonally dependent interannual variability of sea ice in the Bering Sea and its relation to atmospheric fluctuations. J Geophys Res 110(C5):C05011

Stabeno PJ, Schumacher JD, Davis RF, Napp JM (1998) Under-ice observations of water column temperature, salinity and spring phytoplankton dynamics: eastern Bering Sea shelf. J Mar Res 56(1):239–255

Stabeno PJ, Bond NA, Kachel NB, Salo SA, Schumacher JD (2001) On the temporal variability of the physical environment over the southeastern Bering Sea. Fish Oceanogr 10(1):81–98

Steele M, Zhang J, Rothrock D, Stern H (1997) The force balance of sea ice in a numerical model of the Arctic Ocean. J Geophys Res 102(C9):21061–21079

Thorndike AS, Colony R (1982) Sea ice motion in response to geostrophic winds. J Geophys Res 87(C8):5845–5852

Walsh JE, Johnson CM (1979) An analysis of arctic sea ice fluctuations, 1953–77. J Phys Oceanogr 9(3):580–591

Walsh JE, Sater JE (1981) Monthly and seasonal variability in the ocean-ice-atmosphere systems of the North Pacific and the North Atlantic. J Geophys Res 86(C8):7425–7445

Walsh JE, Hibler WD, Ross B (1985) Numerical simulation of northern hemisphere sea ice variability, 1951–1980. J Geophys Res 90(C3): 4847–4865

Zhang J, Rothrock D, Steele M (2000) Recent changes in arctic sea ice: the interplay between ice dynamics and thermodynamics. J Clim 13(17):3099–3114

Zhang J, Woodgate R, Moritz R (2010) Sea ice response to atmospheric and oceanic forcing in the Bering Sea. J Phys Oceanogr 40(8):1729–1747

Zhang Y, Rossow W, Lacis A, Oinas V, Mishchenko M (2004) Calculation of radiative flux profiles from the surface to top-of-atmosphere based on ISCCP and other global data sets: refinements of the radiative transfer model and the input data. J Geophys Res 109:D19

Zhao P, Zhang X, Zhou X, Ikeda M, Yin Y (2004) The sea ice extent anomaly in the north pacific and its impact on the East Asian summer monsoon rainfall. J Clim 17(17):3434–3447